



National Library
of Canada

Acquisitions and
Bibliographic Services Branch

395 Wellington Street
Ottawa, Ontario
K1A 0N4

Bibliothèque nationale
du Canada

Direction des acquisitions et
des services bibliographiques

395, rue Wellington
Ottawa (Ontario)
K1A 0N4

Your file *Votre référence*

Our file *Notre référence*

NOTICE

The quality of this microform is heavily dependent upon the quality of the original thesis submitted for microfilming. Every effort has been made to ensure the highest quality of reproduction possible.

If pages are missing, contact the university which granted the degree.

Some pages may have indistinct print especially if the original pages were typed with a poor typewriter ribbon or if the university sent us an inferior photocopy.

Reproduction in full or in part of this microform is governed by the Canadian Copyright Act, R.S.C. 1970, c. C-30, and subsequent amendments.

AVIS

La qualité de cette microforme dépend grandement de la qualité de la thèse soumise au microfilmage. Nous avons tout fait pour assurer une qualité supérieure de reproduction.

S'il manque des pages, veuillez communiquer avec l'université qui a conféré le grade.

La qualité d'impression de certaines pages peut laisser à désirer, surtout si les pages originales ont été dactylographiées à l'aide d'un ruban usé ou si l'université nous a fait parvenir une photocopie de qualité inférieure.

La reproduction, même partielle, de cette microforme est soumise à la Loi canadienne sur le droit d'auteur, SRC 1970, c. C-30, et ses amendements subséquents.

UNIVERSITY OF ALBERTA

**A Separation Bubble Model for
Low Reynolds Number Airfoil Analysis**

BY



SHUM, Yu Kwong

**A thesis submitted to the Faculty of Graduate Studies and Research in partial fulfillment
of the requirements for the degree of Master of Science.**

DEPARTMENT OF Mechanical Engineering

Edmonton, Alberta

FALL 1992



National Library
of Canada

Bibliothèque nationale
du Canada

Canadian Theses Service Service des thèses canadiennes

Ottawa, Canada
K1A 0N4

The author has granted an irrevocable non-exclusive licence allowing the National Library of Canada to reproduce, loan, distribute or sell copies of his/her thesis by any means and in any form or format, making this thesis available to interested persons.

The author retains ownership of the copyright in his/her thesis. Neither the thesis nor substantial extracts from it may be printed or otherwise reproduced without his/her permission.

L'auteur a accordé une licence irrévocable et non exclusive permettant à la Bibliothèque nationale du Canada de reproduire, prêter, distribuer ou vendre des copies de sa thèse de quelque manière et sous quelque forme que ce soit pour mettre des exemplaires de cette thèse à la disposition des personnes intéressées.

L'auteur conserve la propriété du droit d'auteur qui protège sa thèse. Ni la thèse ni des extraits substantiels de celle-ci ne doivent être imprimés ou autrement reproduits sans son autorisation.

ISBN 0-315-77088-0

Canada

UNIVERSITY OF ALBERTA
RELEASE FORM

NAME OF AUTHOR: **SHUM, Yu Kwong**

TITLE OF THESIS: **A Separation Bubble Model for
Low Reynolds Number Airfoil Analysis**

DEGREE: **Master of Science**

YEAR THIS DEGREE GRANTED: **1992**

Permission is hereby granted to the University of Alberta Library to reproduce single copies of this thesis and to lend or sell such copies for private, scholarly or scientific research purposes only.

The author reserves all other publication and other rights in association with the copyright in the thesis, and expect as hereinbefore provided neither the thesis nor any substantial portion thereof may be printed or otherwise reproduced in any material from whatever without the author's prior written permission.



**409 Buchanan Road
Edmonton Alberta
Canada T6R 2A5**

Dated Aug 24, 1992

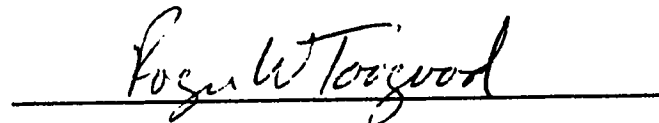
UNIVERSITY OF ALBERTA

FACULTY OF GRADUATE STUDIES AND RESEARCH

The undersigned certify that they have read, and recommend to the Faculty of Graduate Studies and Research for acceptance, a thesis entitled **A Separation Bubble Model for Low Reynolds Number Airfoil Analysis** submitted by **SHUM, Yu Kwong** in partial fulfillment of the requirements for the degree of **Master of Science in Mechanical Engineering**.



Dr. D. J. Marsden (Supervisor)



Dr. R. W. Toogood



Dr. N. Rajaratnam

Dated 19 Aug. 1992

Abstract

Laminar separation bubbles tend to occur on low Reynolds number wing sections (less than $1.5(10^6)$) just prior to the pressure recovery region, as a mechanism of transition from laminar to turbulent boundary layer flow. Since this laminar bubble transition makes an increasingly important contribution to wing section profile drag at low Reynolds number, a model for the analysis of the boundary layer through the bubble is needed. The model developed here is based on Horton's method. It provides a simple and computationally efficient analysis matching the integral boundary layer calculation used in airfoil analysis.

The bubble calculation is initiated by the detection of laminar separation. After transition location is determined using Van Ingen's short-cut e^+ method, which allows the effect of freestream turbulence to be accounted for, the growth in the bubble laminar region is predicted using Schmidt's correlations. The iterative turbulent region calculation was improved by replacing Horton's linear velocity distribution with Wortmann's concave velocity distribution which corresponds better with experimental observations. Both computation efficiency and prediction accuracy were improved by these changes.

Like the original Horton's method, the convergence of the turbulent region iterative calculation means that reattachment can occur and the information generated can initiate the subsequent attached turbulent boundary layer calculation. Bursting is predicted by failure of the turbulent region to reattach.

Addition of the bubble model greatly improved the drag prediction accuracy of airfoil analysis, especially in cases where the mid-chord bubble was a dominant feature on the airfoil. The validity of the bubble model was further confirmed by the good agreement between the calculated values of bubble size, reattachment velocity gradient and their respective measured values, taken from published experimental results on a number of airfoils in the Reynolds number range from $0.2(10^6)$ to $1.5(10^6)$.

Acknowledgement

I wish to thank Dr. D. J. Marsden, my supervisor, for his guidance and supervision. It has been a great pleasure working with him. The grants from NSERC Canada are gratefully acknowledged. Their support was essential for the completion of this work.

Thanks are due to Dr. R. Toogood, Dr. W. Finlay, Mr. A. Wilson, and Mr. C. Merkl for their advice and insights during the progress of the current project. Patience and understanding from my family is appreciated, especially when my brothers, Nelson, and Alex helped prepare the draft of this thesis.

Table of Contents

Chapter 1 Introduction	1
Chapter 2 Airfoil Analysis Without Bubble	7
2.1 Potential Flow	7
2.2 Viscous Flow and Viscous-Inviscid Interaction	12
2.3 Capabilities and Limitations	22
Chapter 3 Bubble Model	24
3.1 General Discussion on Bubble Structure	24
3.2 Horton's Method	26
3.3 Modifications on Laminar Region and Transition Modelling	32
3.4 Modifications on Turbulent Region and Reattachment Modelling	38
Chapter 4 Calibration and Verification	44
4.1 Calibration	44
4.2 Verification	46
Chapter 5 Conclusion	50
Tables	52
Figures	55
References	78

Lists of Tables

Table 1	Comparison of measured and calculated separation location, bubble size on the upper surface for the Eppler 387 airfoil at $Re_c = 0.2(10^6)$	52
Table 2	Comparison of measured and calculated separation location, bubble size on the upper surface for the Eppler 387 airfoil at $Re_c = 0.3(10^6)$	52
Table 3	Calculated Λ_R ranges for various airfoils with $\beta = 0.022$	53
Table 4	Comparison of original and modified Horton's method	54

Lists of Figures

Figure 1	Vortex representation of a single component airfoil	55
Figure 2	Locations of panels on airfoil surface	55
Figure 3	Simulating equivalent airfoil with a trailing edge source	56
Figure 4	Typical velocity profile in boundary layer	56
Figure 5	Correlations between $C_{f, seq}$ and Re_c	56
Figure 6	Boundary layer calculation flow chart	57
Figure 7	Viscous-inviscid interaction	58
Figure 8	Eppler 387 airfoil	59
Figure 9	FX 66-17A-175 airfoil	59
Figure 10	Eppler 387 airfoil at $Re_c = 0.2(10^6)$	59
Figure 11	Eppler 387 airfoil at $Re_c = 0.3(10^6)$	60
Figure 12	Eppler 387 airfoil at $Re_c = 0.46(10^6)$	60
Figure 13	FX 66-17A-175 airfoil at $Re_c = 10^6$	61
Figure 14	FX 66-17A-175 airfoil at $Re_c = 1.5(10^6)$	61
Figure 15	FX 66-17A-175 airfoil at $Re_c = 2(10^6)$	62
Figure 16	Flow structure of a separation bubble	63
Figure 17	Velocity distribution near a separation bubble	63
Figure 18	Velocity distribution of Horton's bubble model	64
Figure 19	Bubble calculation flow chart	64
Figure 20	Expressing I in terms of z	65
Figure 21	Bubble length parameter correction	65
Figure 22	FX 66-S-196 V1 airfoil	66
Figure 23	Eppler 387 airfoil at $Re_c = 0.2(10^6)$	66
Figure 24	Eppler 387 airfoil at $Re_c = 0.3(10^6)$	67
Figure 25	FX 66-17A-175 airfoil at $Re_c = 10^6$	67
Figure 26	FX 66-17A-175 airfoil at $Re_c = 1.5(10^6)$	68
Figure 27	FX 66-S-196 V1 airfoil at $Re_c = 0.5(10^6)$	68
Figure 28	The correlations between C_{dm} and Re_c	69
Figure 29	FX 61-163 airfoil	69

Figure 30	Eppler 403 airfoil	69
Figure 31	FX S02/1-158 airfoil	70
Figure 32	UAG-88-143 airfoil	70
Figure 33	FX LV-152 airfoil	70
Figure 34	Eppler 387 airfoil at $Re_c = 0.46(10^6)$	71
Figure 35	FX 61-163 airfoil at $Re_c = 10^6$	71
Figure 36	FX 61-163 airfoil at $Re_c = 1.5(10^6)$	72
Figure 37	Eppler 403 airfoil at $Re_c = 10^6$	72
Figure 38	FX S02/1-158 airfoil at $Re_c = 10^6$	73
Figure 39	FX S02/1-158 airfoil at $Re_c = 1.5(10^6)$	73
Figure 40	UAG 88-143/20 airfoil at $Re_c = 0.69(10^6)$	74
Figure 41	UAG 88-143/20 airfoil at $Re_c = 10^6$	74
Figure 42	UAG 88-143/20 airfoil at $Re_c = 1.5(10^6)$	75
Figure 43	FX LV 152 airfoil at $Re_c = 0.5(10^6)$	75
Figure 44	Effect of C_{dm} value on the drag prediction of the Eppler 387 airfoil at $Re_c = 0.3(10^6)$	76
Figure 45	Effect of C_{dm} value on the drag prediction of the UAG 88-143/20 airfoil at $Re_c = 10^6$	76
Figure 46	Effect of β value on the drag prediction of the Eppler 387 airfoil at $Re_c = 0.3(10^6)$	77
Figure 47	Effect of β value on the drag prediction of the UAG 88-143/20 airfoil at $Re_c = 10^6$	77

List of Symbols

All length parameters are normalized by c

All velocity parameters are normalized by u_∞

A	amplitude of Tollmien-Schlichting (TS) waves
A_c	amplitude of TS waves at critical point
B	laminar separation angle parameter
c	chord length
C_d	dissipation integral, defined in Eq. (18)
C_D	drag coefficient
C_f	skin friction coefficient, defined in Eq. (18)
C_L	lift coefficient
C_{Mq}	quarter-moment coefficient
C_p	pressure coefficient
C_{pm}	pressure coefficient relative to $u_{e, max}$
C_τ	turbulent shear stress coefficient
D_∞	ratio of entrainment velocity to u_e
f	frequency of disturbance
F	functions, specified in text
H_{12}	boundary layer shape factor, $= \delta_1/\delta_2$
H_{22}	boundary layer shape factor, $= \delta_2/\delta_2$
I	maximum amplification integral, defined in Eq. (64)
K_q	influence matrix coefficient
l	total bubble length
l_1	length of bubble laminar region
l_2	length of bubble turbulent region
m	source strength
	velocity distribution exponent defined in Eq. (73)
n	exponential growth of TS waves in the e^n method
N	number of panels on an airfoil component

P	Gaster's pressure gradient parameter, defined in Eq. (56)
r	radial distance between two points
R_i	right hand side of matrix equation
Re_c	chord Reynolds number, $= u_\infty c / \nu$
Re_{l1}	bubble laminar length Reynolds number, $= u_{eS} l_1 / \nu$
Re_s	distance Reynolds number, $= u_\infty s / \nu$
Re_{δ_1}	displacement thickness Reynolds number, $= u_e \delta_1 / \nu$
Re_{δ_2}	momentum thickness Reynolds number, $= u_e \delta_2 / \nu$
Rt	ratio
s	distance along surface from stagnation point
s_{eq}	equivalent flat plate distance for laminar separation
S_i	matrix coefficient for the trailing edge source
s_{max}	location of peak velocity, $u_{e, max}$
Tu	freestream turbulence level
u	velocity component, tangential to surface
u_e	local external velocity
u_∞	freestream velocity
x, y	Cartesian coordinates
z	transformed length of bubble laminar region, defined in Eq. (62)
α	angle of attack
α_i	spatial amplification rate
β	velocity distribution parameter used in Eq. (72)
γ	vortex density
	dividing streamline angle at laminar separation
Γ	vortex strength
δ	nominal boundary layer thickness
Δ	difference
δ_1	displacement thickness, defined in Eq. (17)
δ_2	momentum thickness, defined in Eq. (17)
δ_3	energy thickness, defined in Eq. (17)
δ_{us}	slope of airfoil surface

η	distance normal to airfoil surface
Λ	pressure gradient parameter, $= \delta_2 / u_e (du_e/ds)$
Λ_2	Pohlhausen parameter, $= \delta_2^2 / \nu (du_e/ds)$
ν	kinematic viscosity
ξ	transformed streamwise coordinate in the η - ξ plane, defined in Eq. (38)
ρ	density
τ	shear stress
ψ	stream function

Superscripts:

$-$	lengths and velocities normalized by δ_{2c} and u_{eS} respectively
\wedge	lengths and velocities normalized by δ_{2T} and u_{eT} respectively

Subscripts:

cr	critical
EQ	equilibrium
i	index of control points
j	index of panel
k	index of airfoil components
m	mean
max	maximum
R	reattachment
s	source
S	laminar separation
sep	turbulent separation
T	transition
TE	trailing edge

Chapter 1 Introduction

Analysis of wing sections operating at low Reynolds number (Re_c) has attracted research attention because of the numerous applications and the difficulty in dealing with laminar separations that occur at low Re_c . Examples of applications include sailplanes [1], [2], human-powered aircraft [3], photovoltaic-powered aircraft [4], high-altitude vehicles [5], [6], and even radio-controlled model planes [7].

Airfoil sections are usually designed with geometrical constraints which may include maximum thickness to chord ratio, surface contour curvature, etc. The UA(2)-180 airfoil [1] was designed to have no concave surface for ease of construction, while Lissaman [4] specified a flat upper surface for his airfoil to enhance the performance of the solar cells. With the geometrical constraints of the airfoil in mind, the designer's task is to maximize the aerodynamic performance. For a low Re_c airfoil, the most important factors to be considered are the pressure recovery and the flow transition mechanism.

Pressure recovery measures how much the flow on the upper surface can decelerate from its velocity peak, $u_{e,max}$, (minimum pressure) to its trailing edge velocity, $u_{e,TE}$. The flow is separated if the pressure recovery is not complete, and the form drag increases substantially. The most famous pressure recovery is the one developed by Stratford [8], [9]. It keeps the flow on the verge of separation by specifying the skin friction, C_f in the pressure recovery region to be zero. It can be identified on the C_p vs x graph as a concave curve, which means the adverse pressure gradient is gradually reduced towards the trailing edge. Besides obtaining reduced drag due to the zero skin friction, the major advantage of Stratford's pressure recovery is that it can finish in the shortest distance. This allows the longest laminar flow before the pressure rise, and thus achieving minimum drag. However, after some numerical experiments, Eppler [10] suggested Stratford's recovery is not optimum in terms of lift generation even though it has the least drag. He found that a pressure recovery less concave than Stratford's can achieve more lift due to a higher roof-top velocity. Kennedy [11] also pointed out

that Stratford's method is not convenient for computation, and he preferred the older Wortmann's [12] pressure recovery. Compared to Stratford's, Wortmann's recovery is likewise maintained on the verge of separation, but it comes with a simpler mathematical relationship using to the boundary layer shape factor, H_{12} , instead of C_f . This allows aerodynamicists the freedom to choose between a moderate recovery and an aggressive recovery by varying H_{12} from 1.8 to 2.4. Kennedy [11] also claimed that Stratford recovery is too conservative because there is almost no difference between Stratford's recovery and Wortmann's recovery with H_{12} equals 1.8. Liebeck [13] had similar idea when he discovered that the original Stratford distribution actually has some reserve from imminent separation. He then introduced the modified Stratford distribution, a more aggressive one, in which the margin from separation in the recovery region is reduced. But both Liebeck [13], and McMasters and Henderson [14] noticed that when angle of attack, α , increases (Re_c decreases) beyond the design condition, the flow with Stratford distribution separates at the start of the recovery region, and an abrupt stall can follow. Their explanation is that Stratford distribution (and the modified one) has constant margin from separation along the whole recovery region. Once the margin is consumed in an off-design condition, the whole recovery region is prone to separation. On the other hand, McMasters and Henderson [14] suggested that an airfoil with Wortmann's recovery has a more gradual stall. It can be said that Stratford's recovery is more accurate than Wortmann's recovery in terms of introducing imminent separation because Stratford's recovery is related to the direct indicator of separation, C_f . Ironically, the accuracy of Stratford's distribution results in poorer stall characteristics.

At low Re_c a laminar flow generally separates when it encounters adverse pressure gradient. After separation, the flow becomes unstable and is prone to transition. Once the flow becomes turbulent, the entrainment of the fluid increases and the flow can have enough energy to reattach back to the airfoil surface. Depending on the amount of adverse pressure gradient and local Reynolds number at separation, Re_c , the three processes, separation, transition, and reattachment can happen in a few percent of chord

length. The resulting flow structure is the separation bubble, or short bubble. With increasing α , accompanied by steep adverse pressure gradient and low Re_c , the flow cannot reattach in a short distance and so the bubble extends to become a long bubble. If the angle of attack continues to increase, the flow can eventually fail to reattach and the bubble bursts. Both Ward [15], and Tani [16] carried out an extensive survey of the experimental observations on the two types of bubbles and the bursting phenomenon. Notably, they classified a bubble which affects only the local pressure distribution as a short bubble, while one which can cause the collapse of the suction peak and consequently the loss of lift as a long bubble. Long bubbles and their bursting are definitely undesirable because they destroy lift drastically and cause dangerously abrupt stall characteristics [16]. However, there is still some debate on whether a short bubble is desirable. Mørnsden [1], Drela [3], and Gad-el-Hak [17] consider short bubble as an efficient transition mechanism if used in an appropriate situation. But Selig [7] pointed out that bubble is an unreliable feature due to its dependence of turbulent intensity and its hysteresis behaviour. Over-prediction of airfoil performance can happen because wind tunnel noises reduce the bubble size and consequently the pressure drag. Selig thus suggested using a convex pressure recovery for very low Re_c applications since his investigation showed that bubbles form in conventional concave recovery.

The purpose of a transition mechanism, mentioned in the last paragraph, is to ensure that there is a pressure recovery. It is known that turbulent flow has more energy to resist separation in the adverse pressure gradient typical of the pressure recovery region. On the contrary, laminar flow tends to separate and form a long bubble or even fails to reattach under the same adverse pressure gradient. Therefore, an airfoil designer must introduce some sort of instability to promote transition before the flow meets the pressure recovery region. Wortmann [18] pioneered a solution by shaping the airfoil surface contour to introduce a moderate adverse pressure gradient before the pressure recovery region. This moderate adverse pressure gradient is designed to cause transition instead of separation. Wortmann named this region as the instability range, which is also commonly referred to as a destabilizing region. Horstmann, Quast, and Boermans [19] criticized the instability range on the fact that it is optimum for one Re_c only.

They suggested that increasing Re_c from design condition can cause additional friction drag due to the forward shift of transition, while reducing Re_c from design condition results in a bubble and associated pressure drag. Pfenninger, Vemuru, Mangalam, and Evangelista [20] also pointed out that the instability range has to be extended over most of the chord to function in very low Re_c operation, wasting available pressure recovery. Nevertheless, if operating in moderate low Re_c condition ($Re_c > 0.7(10^6)$), a well-designed instability range has little increase in drag due to the departure from the design condition. Therefore, it still remains popular with airfoil designers who favour its simplicity [1], [21], [22]. Another drawback of instability range is the occurrence of long bubble in operational conditions with low turbulent intensity. This is partially solved by the extension of Wortmann's instability range concept to more than one adverse pressure gradient [23]. The idea is to connect the suction peak and the concave pressure recovery region with a more rounded pressure distribution to allow easier reattachment for the separated shear layer. Usually the bubble size is reduced but not completely eliminated. It is not surprising that the instability range is also called bubble ramp or transition ramp because of the associated flow behaviour.

The instability can also be introduced by a mechanical device, such as roughness bumps, trip wire [24], and zig-zag tape [25], [26]. Of all these, zig-zag tape is the most efficient device. Boermans and Waibel [26] suggested zig-zag tape's effectiveness is due to its ability to generate three-dimensional vortices which promote transition. Although focused on two-dimensional trip wire rather than three-dimensional zig-zag tape, Gibbings, Goksel, and Hall's model [24] still reveals the general behaviour of these mechanical devices. They found that the effective origin of the turbulent boundary layer after tripping is upstream of the trip location. This represents the drag associated with these devices. Usually the device drag is just a little penalty compared to the pressure recovery it saves. The main advantage of zig-zag tape is its negligible cost. It is also reliable even in very low Re_c conditions. But it provides even less flexibility than the instability range because the size of instability range can be designed

to allow shifting of transition (small bubble) in various angles of attack, while zig-zag tape must have transition in a fixed location.

In 1981, Horstmann and Quast [19] introduced a new generation of boundary layer tripping device, the pneumatic tubulator. It ejects ram air through small ducts into the laminar boundary layer, causing three-dimensional disturbances and subsequent transition. Its four advantages over the instability range and conventional tripping devices are:

- a. It is more effective and reliable in causing transition or reducing bubble size, regardless of Re_c .
- b. It is more flexible because it can be turned off if not needed.
- c. It is more powerful because it can reduce bubble size even if installed downstream of separation location.
- d. It has less device drag because the ram air drag is negligible.

The only drawback is its high installation cost. It should be pointed out that Horstmann and Quast recommended the installation of pneumatic tubulator on the lower surface only. Up to this point, the discussion only focuses on the upper surface pressure distribution because it has larger pressure recovery than the bottom surface and thus dominates the airfoil performance. However, the lower surface also has pressure recovery at low angle of attack and requires transition control. It is actually a more difficult problem to control transition on the lower surface because the transition point tends to shift forward suddenly on some airfoils [1], but the solution is neatly provided by the pneumatic tubulator.

The aim of this project was to find a simple model for the (short) separation bubble, so that it could be incorporated into an existing airfoil analysis and design program developed at the University of Alberta [11]. With this modification, the program can supply more information to an airfoil designer who has to choose between instability range and other tripping devices. On the other hand, an engineer who opts to select an airfoil from different catalogues can use the modified program as a unified testing ground, because comparing data contained in various catalogues can be misleading if they were generated in different wind tunnels.

The original program will be described in Chapter 2, followed by the discussion of available bubble models and more recent developments in Chapter 3. Chapter 4 contains the tests of the modified program against wind tunnel data. The comparison will illustrate the limits of the modified program and its improvements over the original program, and will reveal the places where further improvements should be made. All these will then be summarized in Chapter 5.

Chapter 2 Airfoil Analysis Without Bubble

The original airfoil analysis program was developed by Kennedy and Marsden at the University of Alberta and was fully documented in [11], [27]. This chapter will give a brief review of this program.

The analysis is based on viscous-inviscid interaction. The inviscid (potential) flow is calculated with the vortex panel (boundary element) method, which will be discussed in section 2.1. The viscous flow is calculated with the integral equations of subsonic boundary layers. The coupling of these two calculations is then achieved by iterative calculation. Both the viscous flow calculation and the viscous-inviscid interaction will be discussed in section 2.2. This program's capabilities and limitations will be described in section 2.3.

2.1 Potential Flow

Figure 1 shows an airfoil without a boundary layer. The flow field around the airfoil can be characterized by the distribution of streamlines. Each streamline is represented by a stream function value, ψ . For two-dimensional, incompressible, irrotational flow ψ must satisfy the Laplace's equation,

$$\frac{\partial^2 \psi}{\partial x^2} + \frac{\partial^2 \psi}{\partial y^2} = 0 \quad (1)$$

This means the induced velocities due to freestream, vortices, sinks, sources, doublets can be superimposed. The analysis is focused on steady flow, so the frame of reference can be chosen as the one moving with the airfoil.

Only one streamline, with stream function ψ_k , hits the airfoil in Figure 1, while others simply detour and avoid the airfoil. That streamline splits into two paths at the stagnation point, where it hits the airfoil. Going along the upper and lower surface of the airfoil, the two paths join together and depart from the airfoil right at the trailing

edge, thus satisfying the Kutta condition. Therefore, the entire airfoil surface has the same stream function value, ψ_k .

Dimensional analysis shows that the airfoil surface velocity u_s is equivalent to vortex density, γ . Panel method models an airfoil and its surrounding flow field by placing vortex elements with strength γ on the airfoil surface contour.

To calculate the velocity distribution on the airfoil using panel method, Kennedy and Marsden [27] divided the airfoil surface into a number of panels. An example is shown in Figure 2. Smaller panels are used near the leading edge and the trailing edge to capture the larger velocity gradient and to enhance the stability of the calculation. Kennedy [11] concluded that using straight line panels with constant γ is accurate enough for engineering use, and it saves substantial computation time when compared to using higher order panels.

Each panel mid-point, also referred to as a control point, is represented by a cross in Figure 2. All control points have the same stream function value ψ_k because they are on the same airfoil surface. By superposition, ψ_k is the sum of the induced stream function values from the freestream and all the vortex panels, including the one where the cross is located.

The stream function for a uniform free stream incident to the positive x axis at an angle α is give by,

$$\psi = y \cos \alpha - x \sin \alpha \quad (2)$$

On the other hand, the induced stream function value from a point vortex of strength Γ located at a distance r away is,

$$\psi = \frac{-\Gamma}{2\pi} \ln(r) \quad (3)$$

Integrating Eq. (3) on a panel j gives the stream function value it induces on any control point i as,

$$\psi = \frac{-1}{2\pi} \int_{s_j} \gamma(s_j) \ln[r_{ij}(s_j)] ds_j \quad (4)$$

where s measures the distance along the airfoil surface from the stagnation point, r_{ij} is the distance between the panel j and the control point i .

Consequently, for each control point located at (x_i, y_i) , its stream function value can be obtained by combining Eq. (2) and Eq. (4):

$$\psi_k = y_i \cos \alpha - x_i \sin \alpha - \sum_{j=1}^N \frac{1}{2\pi} \int_{s_j} \gamma(s_j) \ln[r_{ij}(s_j)] ds_j \quad (5)$$

where N is the number of panels on that airfoils.

Using constant γ for each panel and after some rearranging, Eq. (5) can be written as,

$$\psi_k + \sum_{j=1}^N \gamma_j K_{ij} = R_i \quad (6)$$

where

$$R_i = y_i \cos \alpha - x_i \sin \alpha \quad (7)$$

and

$$K_{ij} = \frac{1}{2\pi} \int_{s_j} \ln[r_{ij}(s_j)] ds_j \quad (8)$$

Each of the N panels can provide an equation like Eq. (6), but there are $N + 1$ unknowns. They include the surface stream function, ψ_k , and N panel vortex densities, γ_j 's with $j = 1$ to N . Therefore, one more equation is needed and it is provided by the Kutta condition. To obtain this equation, Kennedy and Marsden [27] specified a point just behind the trailing edge through which the surface streamline must pass. This is not difficult provided that the trailing edge has no thickness. Thus, this point has the same stream function value, ψ_k , as all other control points. Moreover, it can provide the Kutta

condition equation in the form of Eq. (6) with $i = N + 1$. With the number of equations matching the number of unknowns, the system of equations can be written as,

$$\begin{array}{l}
 i=1 \\
 \vdots \\
 \vdots \\
 \vdots \\
 i=N \\
 i=N+1
 \end{array}
 \begin{bmatrix}
 K_{1,1} & \dots & \dots & K_{1,N} & 1 \\
 \vdots & & & \vdots & \vdots \\
 \vdots & & & \vdots & \vdots \\
 \vdots & & & \vdots & \vdots \\
 K_{N,1} & \dots & \dots & K_{N,N} & 1 \\
 K_{N+1,1} & \dots & \dots & K_{N+1,N} & 1
 \end{bmatrix}
 \begin{bmatrix}
 \gamma_1 \\
 \vdots \\
 \vdots \\
 \vdots \\
 \gamma_N \\
 \psi_1
 \end{bmatrix}
 =
 \begin{bmatrix}
 \\
 \\
 \\
 \\
 \\
 \\
 \end{bmatrix}
 \quad (9)$$

The matrix in Eq. (9) is called the influence matrix. As defined in Eq. (8), the influence coefficients, K_{ij} , depend only on the geometry of the airfoil. Straight line panels with constant γ allow the K_{ij} to be expressed in analytical form and thus save computation time by avoiding numerical integration. Once generated, K_{ij} can be reused for various α because only the right hand side of the system R_i is dependent on α .

γ_i , equivalent to $u_{e,i}$ can be solved from Eq. (9) by Gaussian elimination. For subsonic flow, $u_{e,i}$ can then be converted to pressure coefficient, $C_{p,i}$ by the simplified Bernoulli equation:

$$C_p = 1 - \left(\frac{u_e}{u_\infty} \right)^2 \quad (10)$$

where u_∞ is the freestream velocity. With the C_p distributions known, the lift coefficient C_L and the quarter moment coefficient C_{Mq} can then be calculated from numerical integration.

Panel methods generally need more computation time for the same analysis than transformation methods. This is due to the need to solve a matrix when using a panel method. However, the main advantage of the panel method is that it can be easily extended to analyze airfoils with more than one component. Interested readers can refer to Kennedy and Marsden [27] for further details. Until this point drag has not been mentioned because there is no consideration of viscous forces in potential flow.

Therefore, pressure distribution plots, C_p vs x , at various α 's and the C_L vs α plot are the only results one can get from potential flow analysis.

Potential flow calculation can be applied to practical airfoil analysis because viscous force is virtually negligible beyond the boundary layer. Consequently, the flow velocity just outside the boundary layer, u_e , can be determined from the panel method. However, the assumption that the thickness at the trailing edge of the airfoil is zero becomes weaker as the boundary layer thickness is no longer negligible after growth on both surfaces. Both Toogood [28], Moktarian and Modi [29] have shown that it is possible to correct this problem by adding a source to the airfoil trailing edge (see Figure 3).

The induced stream function at (x, y) due to a point source of strength m located at (x_s, y_s) can be written as,

$$\psi = \frac{m}{2\pi} \tan^{-1} \left(\frac{y - y_s}{x - x_s} \right) \quad (11)$$

The effect of the source can be included in the summation for the stream function for each control point (x, y) by rewriting Eq. (6) as,

$$\psi_k + \sum_{j=1}^N \gamma_j K_{ij} + m S_i = R_i \quad (12)$$

where

$$S_i = \frac{-1}{2\pi} \tan^{-1} \left(\frac{y_i - y_s}{x_i - x_s} \right) \quad (13)$$

Now, there are $N + 2$ unknowns, including ψ_k , N of γ_i 's, and m . Besides the N equations supplied by the N panel control points, two more equations are required to solve the system. Again, these two equations are supplied by the Kutta condition. To satisfy the Kutta condition, the surface streamline is specified to pass through two additional control points near the trailing edge. As shown in Figure 3, they locate immediately beyond the boundary layer displacement of the upper and lower surfaces

respectively. With index $i = N + 1$ and $N + 2$, these two Kutta condition control points supply two equations in the form of Eq. (12). The system of equations can thus be written as,

$$\begin{array}{l}
 i=1, \text{ panel} \\
 \vdots \\
 \vdots \\
 \vdots \\
 i=N, \text{ panel} \\
 i=N+1, \text{ KuttaC.1} \\
 i=N+2, \text{ KuttaC.2}
 \end{array}
 \begin{bmatrix}
 K_{1,1} & \dots & \dots & K_{1,N} & S_1 & 1 \\
 \vdots & & & \vdots & \vdots & \vdots \\
 \vdots & & & \vdots & \vdots & \vdots \\
 \vdots & & & \vdots & \vdots & \vdots \\
 K_{N,1} & \dots & \dots & K_{N,N} & S_N & 1 \\
 K_{N+1,1} & \dots & \dots & K_{N+1,N} & S_{N+1} & 1 \\
 K_{N+2,1} & \dots & \dots & K_{N+2,N} & S_{N+2} & 1
 \end{bmatrix}
 \begin{bmatrix}
 \gamma_1 \\
 \vdots \\
 \vdots \\
 \vdots \\
 \gamma_N \\
 m \\
 \psi_k
 \end{bmatrix}
 =
 \begin{bmatrix}
 \vdots \\
 \vdots \\
 \vdots \\
 \vdots \\
 \vdots \\
 \vdots \\
 \vdots
 \end{bmatrix}
 \quad (14)$$

which can be solved by Gaussian elimination.

However, due to the presence of the source, γ_i is not equivalent to u_e . At each control point i , $u_{e,i}$ has to be calculated from the summation of all the induced velocities from the freestream, the source and all the panels. Fortunately the computation time for the summation is minimal compared to that for solving the matrix. Again, C_p can be calculated from the corresponding u_e by using Eq. (10). C_L can then be calculated by integrating the C_p 's numerically.

2.2 Viscous Flow and Viscous-Inviscid Interaction

Lift and drag are the two most important performance parameters in which aerodynamicists are interested. Unlike lift, drag cannot be estimated accurately by integrating the pressure distribution around the airfoil due to its relatively small magnitude. Moreover, the pressure distribution is generated from panel method which is based on inviscid flow, a definite conflict to the idea of drag. Fortunately, for the majority of the airfoil applications, viscous flow can be considered to be confined in the boundary layer. Thus, it should be possible to estimate drag if the growth of the boundary layer is known.

The concept of the boundary layer was first proposed by Prandtl in 1904. The boundary layer is the region where the flow velocity increases gradually from zero (no slip condition) on the airfoil surface to u_e in the inviscid far field. Although the boundary layer has finite thickness, it is so thin that it can be assumed to have no pressure gradient normal to the surface. In other words, C_p is independent of the normal distance from the airfoil surface, η , in the boundary layer. This is particularly true for attached flow with Re_c larger than $0.1(10^6)$, the range of most aeronautical applications. The concept is important because it reduces the Navier-Stokes equations into a more manageable form.

Kennedy's [11] program is based on the following two boundary layer integral equations:

$$\frac{d\delta_2}{ds} = \frac{C_f}{2} - (2 + H_{12}) \frac{\delta_2}{u_e} \frac{du_e}{ds} \quad (15)$$

and

$$\frac{d\delta_3}{ds} = C_d - \frac{3\delta_3}{u_e} \frac{du_e}{ds} \quad (16)$$

Both Eq's. (15) and (16) are the result of integrating the simplified Navier-Stokes equations in the direction normal to the airfoil surface. It should be noted that instead of the Cartesian x - y system used in the inviscid flow calculation, an s - η coordinate system has been employed in the boundary layer calculation with s measures the distance along the airfoil surface from the stagnation point. Since no suction or blowing is considered, only u , the velocity component tangential to the airfoil surface appears in Eq's. (15) and (16). u , varying with η , has its value ranged from 0 on the airfoil surface to u_e at the edge of the boundary layer (see Figure 4). The rest of the parameters in Eq's. (15) and (16) plus some other related parameters will be given in the following paragraphs.

δ_1 , δ_2 , δ_3 are the displacement thickness, momentum thickness and energy thickness respectively, and they are defined as,

$$\begin{aligned}\delta_1 &= \int_0^{\infty} \left(1 - \frac{u}{u_e}\right) d\eta \\ \delta_2 &= \int_0^{\infty} \frac{u}{u_e} \left(1 - \frac{u}{u_e}\right) d\eta \\ \delta_3 &= \int_0^{\infty} \frac{u}{u_e} \left[1 - \left(\frac{u}{u_e}\right)^2\right] d\eta\end{aligned}\tag{17}$$

The skin friction coefficient, C_f , and the dissipation integral, C_d , are defined by,

$$\begin{aligned}C_f &= \frac{2\tau}{\rho u_e^2} \Big|_{\eta=0} \\ C_d &= \frac{2 \int_0^{\infty} \tau \frac{\partial u}{\partial \eta} d\eta}{\rho u_e^3}\end{aligned}\tag{18}$$

where τ is the shear stress, and ρ is the density.

The boundary layer shape factors H_{12} , and H_{32} are defined by,

$$\begin{aligned}H_{12} &= \frac{\delta_1}{\delta_2} \\ H_{32} &= \frac{\delta_3}{\delta_2}\end{aligned}\tag{19}$$

Both the upper and lower surfaces are divided into steps, and Kennedy [11] found that a stepsize of 0.5% chord is sufficient for the analysis. For each surface, the boundary layer calculation starts at the stagnation point and proceeds downstream by integrating both Eq's. (15) and (16) simultaneously. The location of stagnation point has

been determined by the panel method. Following Kennedy [11], the initial values for δ_2 , and δ_3 at stagnation point are determined by:

$$\delta_2|_{s=0} = \frac{0.292}{\sqrt{Re_c \frac{du_e}{ds}}} \quad (20)$$

$$\delta_3|_{s=0} = \frac{0.475}{\sqrt{Re_c \frac{du_e}{ds}}}$$

Consequently, at each step, the values of δ_2 , and δ_3 are obtained from the integration. H_{32} can then be calculated from Eq. (19). The other parameters are provided by empirical correlations which express H_{12} , C_f , C_d in term of H_{32} and Re_{δ_2} . Kennedy used Eppler's correlations [30] for laminar flow, and Felsch, Geropp, and Walz's [31] for turbulent flow. With H_{12} known, δ_1 can be found using Eq. (19). However, it is found that the accuracy of the turbulent flow correlations falls off with decreasing Re_c . Therefore, in this project they are replaced by Drela and Giles' [32] newer correlations, which have been tailored for subsonic flow by Dini [33]. These new correlations are more accurate even at low Re_c , and more efficient in terms of computation time. The improved performance comes from a better modelling of the wake layer Reynolds stresses, which are known to have relatively slow response to changing flow conditions, particularly at low Re_c . Drela and Giles achieve this by using the turbulence lag equation:

$$\frac{\delta}{C_\tau} \frac{dC_\tau}{ds} = 4.2 (\sqrt{C_{\tau,EQ}} - \sqrt{C_\tau}) \quad (21)$$

where δ is the nominal boundary layer thickness. C_τ , the turbulent shear stress coefficient, is a measure of the Reynolds stresses in the wake layer. If the pressure gradient changes slowly, C_τ should follow its equilibrium value, $C_{\tau,EQ}$ closely, but usually the lagging is too large to be ignored. In the form of an integral equation, Eq. (21)

accounts for the Reynolds stresses' dependence on the flow history and thus simulates the lagging. Drela and Giles' correlations express $C_{\tau, EQ}$, δ , H_{12} , C_f , C_d in term of H_{32} and Re_{δ_2} . These expressions provide the closure to the three equations, Eq's. (15), (16) and (21), which can then be integrated simultaneously downstream.

The switch from laminar flow calculation to turbulent flow calculation is triggered by the detection of natural transition or laminar separation. In other words, the bubble development behind laminar separation is ignored and immediate transition is assumed. Also, Kennedy [11] points out that it is more practical to model the transition at a point, although transition is actually a gradual process which takes a finite distance to finish. The criteria for natural transition will be discussed in the following paragraphs, followed by that for laminar separation.

To predict natural transition, Kennedy [11] originally used White's criterion [34] which states that transition occurs when,

$$Re_{\delta_2} \geq 2.9 Re_s^{0.4} \quad (22)$$

Similar to the more well-known Michel's criterion, White's criterion is very convenient to use, but lacks flexibility because it has not considered the effect of freestream turbulence and surface roughness. Therefore, White's criterion is replaced with the more complicated but flexible e^n method.

The e^n method predicts transition by relating the phenomenon to the linear spatial amplification of Tollmien-Schlichting (TS) waves. Transition occurs when the exponential growth of TS waves, represented by n , exceeds the limit, n_T . Finlay [35] points out that e^n method works well for airfoil analysis because non-linear amplification of TS waves only occurs in the neighbourhood of transition location and can thus be ignored in the initial growth.

As Arnal [36] explains, significant TS wave growth starts only after the boundary layer reaches a critical thickness, or when $Re_{\delta_2} \geq Re_{\delta_2, cr}$. Writing A as the amplitude of TS waves and A_0 as the amplitude at critical point, the amplification ratio, A/A_0 , can then be calculated using linear stability theory according to the disturbance

frequency, f , and the boundary layer thickness parameter, $Re_{\delta l}$ for a velocity profile with a constant H_{12} :

$$\ln\left(\frac{A}{A_0}\right) = F_1(f, Re_{\delta l}), \quad \text{const. } H_{12} \quad (23)$$

For any combination of $Re_{\delta l}$ and H_{12} , there is only one unique f for which the amplification is maximum. Since n is defined as the natural log of that maximum amplification ratio, the envelope of all these amplification curves for different f represents some correlations between n , H_{12} , $Re_{\delta l}$. In mathematical terms, the relationship between the growth of TS waves (n), and the boundary layer status (H_{12} , $Re_{\delta l}$) can be written as,

$$n = \max \left[\ln\left(\frac{A}{A_0}\right) \right] = F_2(H_{12}, Re_{\delta l}) \quad (24)$$

A notable application of the e^n method comes from Van Ingen, and Boermans [25], who reduce the correlations between TS wave amplification and boundary layer status to a database of about 300 numbers. However, it has been suggested that using this database requires substantial computation time, and so a simpler model is used in the current project. Van Ingen, and Boermans [25] also provide a correlation between n_T and freestream turbulence level, Tu , and suggest n_T should vary from 10 (wind tunnel) to 15 (free-flight).

The e^n method chosen for the current project was developed by Gleyzes, Cousteix, and Bonnet [37], who used a straight line fit on the envelope of the amplification curves. This approximation allows the correlations between n , H_{12} , and $Re_{\delta 2}$ to be written in a very convenient format:

$$\frac{dn}{dRe_{\delta 1}} = \begin{cases} 0.016433H_{12} - 0.038145, & H_{12} \leq 3.35 \\ -0.009988H_{12}^2 + 0.075774H_{12} - 0.124776, & H_{12} > 3.35 \end{cases} \quad (25)$$

Cousteix [38] reveals the correlation between $Re_{\delta 2,cr}$ and H_{12} as,

$$Re_{\delta 2,cr} = \begin{cases} \frac{\exp\left(5.27 + 17.2 \sqrt{\frac{1}{H_{12}} - 0.39}\right)}{H_{12}} & H_{12} \leq 2.5 \\ \frac{\exp\left(3.5 + \frac{2.897}{H_{12}} + \frac{22230}{H_{12}^{10}}\right)}{H_{12}} & H_{12} > 2.5 \end{cases} \quad (26)$$

In each step of the boundary layer calculation, $Re_{\delta 2}$ is checked if it has exceeded $Re_{\delta 2,cr}$. Once it is true, the calculation can then include the integration of Eq. (25), which can be carried on until n is larger than n_γ . This procedure was incorporated into the boundary layer calculation and the extra computation time was found to be negligible.

The laminar separation criteria used by Kennedy [11] are still used in the current project. One was developed by Liu and Sandborn [39]. It states that laminar separation happens when,

$$H_{12} \geq 3.2 \exp(-17.5 \Lambda_2) + 3.1 \quad (27)$$

where Λ_2 , the Pohlhausen parameter, is defined by,

$$\Lambda_2 = \frac{\delta_2^2}{\nu} \frac{du_e}{ds} \quad (28)$$

Another criterion, developed by Curle and Skan [40], states that laminar separation occurs when,

$$C_{pm} \left(s_{eq} \frac{\partial C_{pm}}{\partial s} \right)^2 \geq 0.0104 \quad (29)$$

where C_{pm} is defined by,

$$C_{pm} = 1 - \left(\frac{u_e}{u_{e,max}} \right)^2 \quad (30)$$

and s_{eq} can be calculated from,

$$s_{eq} = \frac{u_e}{\nu} \left(\frac{\delta_2}{0.664} \right)^2 \Big|_{s=s_{max}} + (s - s_{max}) \quad (31)$$

s_{max} in Eq. (31) represents the location where u_e is at its maximum. Therefore, the first term in Eq. (31) is the equivalent length of a flat plate required for the same δ_2 at the velocity peak, and the terms in the bracket then represent the length of surface under adverse pressure gradient. Laminar separation is assumed to occur if either Eq. (27) or Eq. (29) becomes true.

Since Kennedy did not use any laminar separation bubble model, the boundary layer integral calculation in the original program was immediately switched to the turbulent branch if natural transition or laminar separation was detected. Kennedy [11] assumed the continuity of δ_2 , and δ_3 after transition or laminar separation. This assumption agrees with the fact that δ_1 drops considerably after transition. In the current project, the immediate transition mechanism is replaced by a more genuine bubble model for laminar separation. The bubble model will be detailed in Chapter 3.

The turbulent boundary layer calculation can be carried on to the trailing edge of the airfoil, or it can stop at the turbulent separation location. The criteria for turbulent separation is somewhat arbitrary and less reliable than that for transition or laminar separation. It states that,

$$C_f \leq C_{f, sep}(Re_c) \quad (32)$$

Figure 5 shows the relationship between $C_{f, sep}$ and Re_c . The relationship was determined by correlations of published experimental data and should provide reasonable accuracy if separation occurs after mid-chord. The reduced lift due to trailing edge separation is accounted for using a formula developed by Eppler [10]:

$$\Delta C_L = -\pi \left(\frac{L_{sep}}{c} \right) (\delta_{us} + \alpha) \quad (33)$$

where L_{sep} represents the length of the separated region and δ_{us} is the slope of the airfoil upper surface at trailing edge. It is assumed that δ , then grows at a linear rate after turbulent separation, so that a value of δ , at the trailing edge can be obtained for the calculation of drag of the airfoil. This model of trailing edge separation is of course very primitive, but it is adopted for this project due to its simplicity. Readers interested in this topic can refer to Blascovich [41], Drela and Giles [32] for more recent and advanced models for turbulent separated flow.

The purpose of the boundary layer calculation is to predict the drag coefficient, C_D , of the airfoil. The widely used Squire and Young formula [42] gives a correlation between C_D and the trailing edge condition on each surface as:

$$C_{D, surface} = 2 \left(\frac{\delta_2}{c} \right) \left(\frac{u_e}{u_\infty} \right)^{\left(\frac{H_{12}}{2} + 2.5 \right)} \Bigg|_{TE} \quad (34)$$

For single component airfoil, the total C_D is due to the drag on both surfaces:

$$C_D = C_{D, up} + C_{D, low} \quad (35)$$

The boundary layer calculation can be summarized in the flow chart in Figure 6. It shows that the calculation only requires the velocity distribution (u_e 's) around the airfoil as input, and produces two major outputs:

- a. the airfoil C_D ,

b. δ_i 's around the airfoil.

Those δ_i distributions are used for viscous-inviscid coupling, which is the subject of the rest of the section. It should be noted that the bubble model would be incorporated in the calculation by replacing the dashed line in Figure 6.

As explained earlier, the panel method can be applied to practical airfoil analysis because viscous flow is confined in the thin boundary layer. The original airfoil, with its shape displaced due to the presence of the boundary layer, can thus be represented by an equivalent airfoil. Figure 3 shows an original airfoil (solid line) and its equivalent airfoil (dashed line). The application of the panel method on the equivalent airfoil, which has a trailing edge with finite thickness, has been discussed in section 2.1. The biggest deviation of the equivalent airfoil from the original one is its reduced camber, caused by the thicker boundary layer on the upper surface. Therefore, failing to use the equivalent airfoil for analysis can lead to overestimation of C_L because the reduced camber of the airfoil has not been accounted for.

It is not exaggerating to say that the concept of equivalent airfoil is the key to viscous-inviscid interaction because it provides a feedback route from the boundary layer calculation to the potential flow calculation. This allows the use of an iteration loop to couple the two types of calculation.

Figure 7 is a flow chart for the viscous-inviscid coupling procedure, which is explained as follows. Velocity (u_e) distribution is obtained from the original airfoil coordinates using the panel method. The u_e distribution is the input to the boundary layer calculation, which has been illustrated in detail in Figure 6. The equivalent airfoil (Figure 3) is simulated by displacing the original airfoil surface normally outward by an amount equal to the local δ_i value, which is produced from the boundary layer calculation. Again, a new u_e distribution can be obtained from the equivalent airfoil coordinates using the panel method. After that, the three processes (boundary layer calculation, equivalent airfoil simulation, and the panel method) form an iteration loop. The looping is repeated until both C_L (from panel method), and C_D (from boundary layer calculation) converge within their respective tolerances.

2.3 Capabilities and Limitations

The performance of the original code can be demonstrated by comparing the results it produces with available experimental data. Two airfoils are selected for the demonstration. The first one is the Eppler 387 airfoil (see Figure 8), which was designed for low Re_c ($0.5(10^6)$) application. Its performance data can be obtained from McGhee, Walker, and Millard [43], who have carried out an extensive testing program on this airfoil. The second one is the FX 66-17A-175 airfoil (see Figure 9) by Wortmann. It was designed for general aviation purposes with $Re_c > 10^6$. Its coordinates and performance data are contained in the catalogue by Althaus and Wortmann [44].

The calculated results for the Eppler 387 airfoil are shown with the experimental data at $Re_c = 0.2(10^6)$, $0.3(10^6)$, $0.46(10^6)$ in Figure 10, Figure 11, and Figure 12 respectively. McGhee et. al. [43] suggest that the tests were carried out in the NASA Langley low-turbulence pressure tunnel at $Tu = 0.055\%$, so the value of n_T is chosen to be 11.2 according to Van Ingen et. al. [25]. It can be seen in Figure 12 that the agreement between experimental data and calculated results is excellent at $Re_c = 0.46(10^6)$. However, the agreement deteriorates with decreasing Re_c . Figure 11 shows that C_D is under-predicted by about 0.0007 at $Re_c = 0.3(10^6)$ over the practical C_L range between 0.35 and 1.05, while Figure 10 shows that C_D is under-predicted by about 0.0015 at $Re_c = 0.2(10^6)$ over the same C_L range. The calculated results suggest that laminar separation occurs in every α tested. Thus it is apparent that the bubble size grows and becomes more dominant when Re_c drops below $0.4(10^6)$.

Similarly, the calculated results for the FX 66-17A-175 airfoil are shown with the experimental data at $Re_c = 10^6$, $1.5(10^6)$, $2(10^6)$ in Figure 13, Figure 14, and Figure 15 respectively. The value of n_T was chosen to be 14 because Althaus et. al. [44] claim that the Laminar Wind Tunnel of the University of Stuttgart (Stuttgart LWT) has a very low Tu of less than 0.02%. Again, as shown in Figure 15, the agreement between calculated results and experimental data is excellent at $Re_c = 2(10^6)$, but deteriorates with decreasing Re_c . The calculated results show that in the practical C_L range between 0.2

and 1.4, laminar separation only occurs on the upper surface because of the larger adverse pressure gradient. Thus it is the separation bubble on the upper surface causing the substantial drag increases. As shown in Figure 13 ($Re_c = 10^6$), C_D is under-predicted by more than 0.001 at lower C_L and by about 0.0007 at higher C_L because the bubble size is reduced at higher α . A similar trend can also be observed in Figure 14 ($Re_c = 1.5(10^6)$), although the bubble is causing less drag increases.

From the above two test cases, it can be seen that separation bubble can grow quickly and cause substantial drag increases if Re_c drops below the value which the airfoil was designed for. Therefore, to improve the accuracy of drag prediction at low Re_c , the "immediate transition" assumption must be replaced with a better separation bubble model. The search for such a bubble model and how it is incorporated into the original code will be discussed in Chapter 3.

Chapter 3 Bubble Model

This chapter contains the details of the separation bubble model, which forms the core of the current project. It is based on the bubble model developed by Horton [45] in 1967. He obtained the boundary layer growth in bubbles by integrating both Eq's. (15) and (16) manually. Also, Horton's method only requires the boundary layer information upstream of separation point. It was adopted for the current project because it is convenient to use. There have been more than two decades of advancements in both experimental observation and theoretical analysis on separation bubbles since 1967. Thus, it was expected that this classical method could be improved to make it a simple and reliable tool for bubble analysis. Consequently, this chapter is divided into four parts. Section 3.1 will contain some general discussion on bubble structure, followed by the development of the original Horton's method in section 3.2. The modifications on Horton's method will be discussed in sections 3.3 and 3.4.

3.1 General Discussion on Bubble Structure

A simple sketch of a laminar separation bubble is shown in Figure 16. It is a short bubble which is characterized by a quickly reattaching turbulent shear layer. The bubble starts at point S, where the attached laminar boundary layer separates to form the shear layer. The shear layer is very unstable and disturbances grow quickly. This eventually leads to transition at point T. After the shear layer turns turbulent, the increased entrainment and mixing with the exterior flow cause the reattachment at point R, where the bubble ends. For convenience, the subscripts *S*, *T*, *R* will be used to represent separation, transition, and reattachment respectively in the following text.

The solid streamline in Figure 16 is the dividing streamline which divides the bubble region into the outer shear layer and the inner flow reversal region. Schmidt [46] points out that the turbulent shear layer expands quickly as momentum is transferred from the external flow. Compared to an attached turbulent boundary layer, the turbulent shear layer causes more airfoil drag by yielding a thicker boundary layer

after reattachment. On the other hand, the inner flow reversal actually reduces airfoil drag by providing negative C_f . When Re_c is higher than 10^6 , the bubble can be short enough that the increase in drag due to shear layer entrainment is cancelled or even overcome by the reduction of drag due to flow reversal. However, as the bubble grows longer with decreasing Re_c , the entrainment and its associated drag will dominate. Eppler [10] supplies a rule of thumb to determine whether a bubble will add more drag to the airfoil. It states that there is negligible drag penalty if,

$$\frac{u_{eS} - u_{eR}}{u_{eS}} < 0.042 \quad (36)$$

In other words, a separation bubble can be used as an efficient transition mechanism if its size is within the limit suggested in Eq. (36).

Figure 17 shows the perturbation on the surface velocity distribution due to the presence of a bubble. The dashed line represents the u_e distribution when the bubble is eliminated by a boundary layer trip, while the solid line represents the perturbed u_e distribution when the bubble is present. For the bubble case, laminar separation occurs shortly after the flow decelerates. Instead of decelerating steeply as in the tripping case, the flow has its velocity kept at a value very close to u_{eS} until transition occurs. The flat u_e distribution between separation and transition is usually referred by researchers as the "plateau." Van Ingen and Boermans [25] suggest the following correlations for the u_e plateau:

$$\frac{u_e}{u_{eS}} = \begin{cases} 0.978 + 0.022 \exp(-4.545 \xi - 2.5 \xi^2) & 0 \leq \xi \leq 1.3333 \\ 0.978 & \xi > 1.3333 \end{cases} \quad (37)$$

where the transformed streamwise coordinate, ξ , is defined as,

$$\xi = \frac{s - s_S}{\delta_{2S} Re_{\delta_{2S}}} \quad (38)$$

After transition, the turbulent entrainment causes the shear layer to reattach to the airfoil surface with the flow decelerating quickly. In fact, the velocity gradient between

T and R (solid line) is steeper than any segment of the attached flow u_e distribution (dashed line). This also explains the intense growth of the turbulent shear layer.

The perturbation to the u_e distribution is not limited to the region within the bubble. It can be seen in Figure 17 that the velocity peak is reduced due to the presence of the bubble. Also, after reattachment, the flow cannot adjust its velocity quickly enough and this results in some sort of overshooting. The overshooting can bring additional difficulties to researchers who have to determine reattachment location experimentally [47]. For the current project, it is more convenient to define the reattachment location as the intersection point of the solid line and the dashed line as illustrated in Figure 17.

The extent of external perturbation depends heavily on the bubble length. Figure 2c in Ref. [48] shows that the entire u_e distribution can be reduced substantially due to the presence of a long bubble, causing a stall. The current project will concentrate on short bubbles which have most of their perturbation confined to the separation region. Only this type of bubble can act as an efficient transition mechanism without causing drastic degrading in airfoil performance.

3.2 Horton's Method

Horton [45] developed a model for the boundary layer growth in the bubble because he wanted to investigate the bursting phenomenon. Information generated in this model can be used to determine whether bursting will occur. If bursting does not happen and the separated flow reattaches to the airfoil surface, the growth information can then be used to initialize the subsequent turbulent boundary layer calculation for the calculation of airfoil drag (C_D).

Horton assumes that a bubble only perturbs locally within the separated region. Consequently, there is no peak velocity reduction or reattachment overshooting in the perturbed u_e distribution shown in Figure 18. For simplicity, he specifies that u_{eT} is equal to u_{eS} . The more recent correlations in Eq. (37) shows that this is not a bad

assumption at all. Horton also assumes that the laminar shear layer does not grow, so the laminar part of his model can be summarized as:

$$\begin{aligned} u_{eT} &= u_{eS} \\ \delta_{2T} &= \delta_{2S} \end{aligned} \quad (39)$$

This allows Horton to normalize length parameters and velocity parameters with δ_{2S} and u_{eS} respectively. Following Horton's notation, parameters normalized against the separation condition will appear with an overline in the following text. For example, \bar{u}_e represents u_e/u_{eS} .

Horton uses l , l_1 , and l_2 to represent the total length, the length of the laminar region, and the length of the turbulent region of the bubble respectively, so these length parameters can be related to surface distance s as,

$$\begin{aligned} l_1 &= s_T - s_S \\ l_2 &= s_R - s_T \\ l &= l_1 + l_2 = s_R - s_S \end{aligned} \quad (40)$$

He also provides the correlation between \bar{l}_1 and Re_{s2} as,

$$\bar{l}_1 = \frac{l_1}{\delta_{2S}} = \frac{4(10^4)}{Re_{s2}} \quad (41)$$

which does not include the effect of freestream turbulence level.

The essence of Horton's method lies in the model of the turbulent shear layer and its reattachment. As illustrated in Figure 18, Horton assumes that the turbulent shear layer decelerates linearly from T to R , so the external velocity distribution can be written as,

$$\bar{u}_e = 1 - (1 - \bar{u}_{eR}) \left(\frac{\bar{s} - \bar{s}_T}{\bar{l}_2} \right) \quad (42)$$

Differentiating Eq. (42) with \bar{s} gives,

$$\left. \frac{d\bar{u}_e}{d\bar{s}} \right|_R = \frac{\bar{u}_{eR} - 1}{\bar{l}_2} \quad (43)$$

Using Eq. (43), $\bar{\delta}_2$ at reattachment can be expressed as,

$$\bar{\delta}_{2R} = \frac{\Lambda_R \bar{u}_{eR} \bar{l}_2}{\bar{u}_{eR} - 1} \quad (44)$$

with the pressure gradient parameter, Λ , defined by,

$$\Lambda = \left(\frac{\delta_2}{u_e} \frac{du_e}{ds} \right) \quad (45)$$

On the other hand, $\bar{\delta}_{2R}$ can also be expressed in terms of the growth between T and R . First, Horton rewrites Eq. (16) as,

$$\frac{1}{u_e^3} \frac{d}{ds} (u_e^3 H_{32} \delta_2) = C_d \quad (46)$$

Both C_d and H_{32} are assumed to have little change in the turbulent shear layer and thus each can be represented by an overall mean value. Then Eq. (46) can be integrated as,

$$\bar{\delta}_{2R} \bar{u}_{eR}^3 - 1 = \frac{C_{dm}}{H_{32m}} \int_{\bar{s}_T}^{\bar{s}_R} \bar{u}_e^3 d\bar{s} \quad (47)$$

or after some transformation,

$$\bar{\delta}_{2R} = \frac{1}{\bar{u}_{eR}^3} + \frac{C_{dm}/H_{32m}}{\bar{u}_{eR}^3} \int_{\bar{s}_T}^{\bar{s}_R} \bar{u}_e^3 d\bar{s} \quad (48)$$

Upon substituting Eq. (42) and carrying out the integral in Eq. (48), it becomes,

$$\bar{\delta}_{2R} = \frac{1}{\bar{u}_{eR}^3} + \frac{C_{dm}}{4 H_{32m}} \frac{\bar{l}_2 (1 - \bar{u}_{eR}^4)}{\bar{u}_{eR}^3 (1 - \bar{u}_{eR})} \quad (49)$$

By equating Eq. (44) and Eq. (49), Horton finds a relationship between \bar{u}_{eR} and \bar{l}_2 :

$$\bar{u}_{eR}^4 = \frac{\frac{C_{dm}}{4 H_{32m}} + \frac{(1 - \bar{u}_{eR})}{\bar{l}_2}}{\frac{C_{dm}}{4 H_{32m}} - \Lambda_R} \quad (50)$$

But he still has to determine the values of Λ_R , H_{32m} , and C_{dm} .

To find Λ_R , Horton uses Truckenbrodt's shape-parameter equation, which can be derived by combining Eq's. (15) and (16). It states that,

$$\delta_2 \frac{dH_{32}}{ds} = (H_{12} - 1) H_{32} \frac{\delta_2}{u_e} \frac{du_e}{ds} + C_d - \frac{H_{32} C_f}{2} \quad (51)$$

C_f is equal to 0 at reattachment. Also, using some experimental data, Horton concludes that H_{32} reaches minimum at reattachment. This means that,

$$\left. \frac{dH_{32}}{ds} \right|_R = 0 \quad (52)$$

Therefore, at reattachment, Eq. (51) can be reduced to,

$$\Lambda_R = \left(\frac{\delta_2 du_e}{u_e ds} \right)_R = \left(- \frac{C_d}{H_{32}(H_{12} - 1)} \right)_R \quad (53)$$

Eq. (53) implies that Λ_R depends only on the local velocity profile at reattachment. The dependence also holds true for H_{32m} and C_{dm} , although they are subject to some variation because they are actually the mean value between T and R . Horton suggests that there is a universal wake-like velocity profile for short bubble reattachment regardless of the airfoil Re_c , so he tries to find the values of Λ_R , H_{32m} , and C_{dm} by integrating the velocity profile. After some minor adjustments to the theoretical values so that they can correspond better with the experimental data from various sources, Horton suggests the following:

$$\begin{aligned}\Lambda_R &= -0.0082 \\ H_{32m} &= 1.50 \\ C_{dm} &= 0.0182\end{aligned}\tag{54}$$

which can be substituted back into Eq. (50). Another relationship between \bar{u}_{eR} and \bar{l}_2 is of course the u_e distribution from the potential flow calculation. With these two independent relationships, the reattachment location can be solved using the Newton-Raphson method.

After the values of \bar{u}_{eR} and \bar{l}_2 are solved, turbulent boundary layer calculation starts at the reattachment location. The initial values can be derived using Eq. (44) and the reattachment velocity profile. They are,

$$\begin{aligned}\delta_{2R} &= \delta_{2S}(\bar{\delta}_{2R}) = \delta_{2S} \left(\frac{\Lambda_R \bar{u}_{eR} \bar{l}_2}{\bar{u}_{eR} - 1} \right) \\ H_{32R} &= 1.51\end{aligned}\tag{55}$$

On the other hand, if the values of \bar{u}_{eR} and \bar{l}_2 cannot converge, or if the shear layer reattach is at a location beyond the trailing edge of the airfoil, the bubble is assumed to have burst. This means that Horton's method can also function as a bursting criterion.

As illustrated in Figure 19, Horton's bubble model can be incorporated into the boundary layer calculation which has been outlined in Figure 6. The flow chart in Figure 19 thus replaces the dashed line in Figure 6 for bubble calculation. It should be noted that the bubble model was not part of the boundary layer iteration loop in the current project. This is because the sudden increase of δ_i associated with the bubble can cause substantial perturbation to the u_x distribution around the separation location. Since the laminar separation prediction is very sensitive to the local u_x gradient, the perturbation results in serious instabilities in determining the separation location, thus increasing the required number of iterations considerably. Therefore, for the current project, the bubble calculation is only applied after the separation location has been determined via the viscous-inviscid interaction iterative schemes.

Depending on the camber of the particular airfoil, convergence can be achieved within 6 to 8 iterations, with tolerances set at $\Delta C_L < 0.003$ and $\Delta C_D < 0.0003$. Locating the separation position without using the bubble model in the viscous-inviscid interaction is consistent with Horton's assumption that the bubble introduces a local perturbation only. The only penalty for doing so is that a minor error can be introduced in the C_L prediction because the value of δ_i at the trailing edge is smaller than it should be if the bubble has been accounted for. Nevertheless, preliminary testing suggested that the effect on the drag polar (C_L vs C_D) plot is practically negligible.

The original codes were thus modified with the inclusion of Horton's bubble model. After some testing, it was found that the additional computation time due to the iterative scheme is minimal compared to the rest of the boundary layer calculation, suggesting that Horton's method is practical. However, the airfoil C_D was seriously underestimated in every test case. It was believed that the error came from inaccurate prediction of shear layer growth. Therefore, some revisions of Horton's bubble model were necessary before it could become an accurate and reliable tool for low Re_x airfoil analysis. Available models for improvement will be discussed in the following sections.

3.3 Modifications on Laminar Region and Transition Modelling

Dini's [33] calculation scheme represents the most recent development on bubble model. He recognizes the need to communicate flow information from the reattachment region upstream to the separation point. This idea is entirely different from the traditional one that bubble development is solely dependent on the separation condition. Dini argues that reverse flow inside the bubble can actually affect the flow upstream and the bubble model should therefore include the same mechanism. Therefore, Dini uses Gaster's pressure gradient parameter, P , as the feedback mechanism. It is defined by,

$$P = \frac{(\delta_{2s})^2 (u_{eR} - u_{eS})}{\nu (s_R - s_S)} \quad (56)$$

Before the bubble calculation, P cannot be determined because it requires knowledge of reattachment location, s_R , which still remains an unknown. However, P has to be determined before the bubble calculation can proceed because the prescribed H_{32} distribution (will be discussed in section 3.4) is indirectly dependent on P . Thus, a guessed value of P is used to start the bubble calculation. The calculation can determine s_R , and hence produce a new value of P , which can be immediately substituted back to start a new round of bubble calculation. The process is repeated until P converges.

It can be recalled from section 3.2 that Horton's model also contains an iterative scheme, but it is limited to the turbulent region. Compared to Horton's model, Dini's model has its iterative scheme extended to cover the entire bubble. Dini claims that his model is more effective in simulating the upstream influence of bubble. It is speculated that this improvement helps stabilize the computation during a parameter sweep via a better control on the bubble size prediction. Thus the C_L vs C_D plots generated will have a smoother appearance.

Although Dini's bubble model holds the advantage of better accuracy and computation stability, the current project will follow the more traditional scheme, which has iterative calculation confined in the turbulent region only. In other words, the state of the laminar region is calculated directly from the separation condition. Once

determined, it cannot be altered by the subsequent development in the turbulent region. It is believed that this straightforward approach can still produce satisfactory results for engineering purposes and is in better coherence with the simplicity of Horton's method. Also, it is more efficient to "tune" an analysis program against experimental results if it involves fewer empirical parameters.

Horton's claim that the laminar shear layer has zero growth is questioned by Schmidt [46]. By combining Eq. (46), which is the alternate form of the kinetic energy integral equation, and the entrainment equation, which states that,

$$\frac{d}{ds}[u_e(\delta - \delta_l)] = D_w u_e \quad (57)$$

Schmidt shows that the laminar shear can thicken substantially. It should be noted that in Eq. (57), δ is the nominal boundary layer thickness, and $D_w u_e$ is the entrainment velocity. Schmidt explains that using Eq. (57) can reveal the importance of some terms which are usually considered negligible if Eq. (15), the momentum thickness equation is used instead.

Since the laminar shear layer growth is not negligible, a better model of the bubble laminar region should be incorporated into Horton's method to produce more accurate C_D calculation. In fact, there are many from which to choose, and they can be classified into two main types.

The first type is characterized by the extension of the laminar attached flow correlations directly into the separated region. In other words, Eq's. (15) and (16) can be integrated from the stagnation point and continuously up to the transition point in the bubble, eliminating the need to detect laminar separation. A notable example comes from Drela and Giles' [32] laminar flow correlations, which are developed using the Falkner-Skan one-parameter profiles. The transition criterion is accordingly modified so that it can be used in the separated region, and this has been done by Van Ingen et al. [25] and Gleyzes et al. [37]. Both parties' formulations are based on the amplification of TS waves, or the so called e^n method. By combining the laminar flow correlations of Drela et al. [32] with the transition criterion of Gleyzes et al. [37], Coiro and Nicola [49]

demonstrate that excellent agreement with experimental data can be achieved using this type of laminar flow model.

Another type of laminar flow model is considerably simpler. It is characterized by the decoupling of the transition detection from the calculation of laminar shear layer growth. First, the transition criterion is expressed in terms of the information at separation. It is usually based on experimental data. Examples are Horton's original criterion in Eq. (41) and Schmidt's [46] criterion:

$$Re_u = \frac{u_{es} l_1}{\nu} = 2175(Re_{s2, s})^{0.5150} \quad (58)$$

The laminar flow model used in the current project is the short-cut e^n method developed by Van Ingen [50], [25]. It is quite unique because it contains the merits of both types of models mentioned above. Compared to the second type of models which are developed empirically, it is more credible because it is based on the theory of TS waves amplification in the laminar separated flow, and thus the effect of freestream turbulence is also accounted for. On the other hand, it requires substantially less computation time than the first type of laminar flow model. For these reasons, it was adopted for the current project as a compromise between computation ease and accuracy.

It is worthwhile to go through the development of this short-cut e^n method because it can help review all the essential features in the laminar part of the bubble. Using linear stability theory, the amplification ratio of TS waves, A/A_o , can be expressed as,

$$n = \max \left[\ln \left(\frac{A}{A_o} \right) \right] = \max \left[\int_{s_o}^s -\alpha_i ds \right] \quad (59)$$

where α_i is the spatial amplification rate. The maximum function in Eq. (59) implies that for any combination of shear layer thickness (Re_{s1}) and profile (H_{12}), there is a disturbance frequency at which the amplification goes to maximum. As in attached flow, transition happens when n is accumulated to exceed a prescribed limit, n_T .

Rather than expressing n into a function of Re_{δ_1} and $H_{1,2}$ as in Eq. (24), Van Ingen [50] chooses to evaluate n by integrating Eq. (59) directly at various frequencies, f . However, to simplify the calculation, he has to make the following assumptions:

- 1) $u_e, \delta_2, Re_{\delta_2}$ stay unchanged after separation, so the normalized frequency $2\pi f\delta_2/u_e$ can be treated as constant during the evaluation of the integral in Eq. (59) for each f .
- 2) No appreciable amplification occurs prior to separation.
- 3) $-\alpha_1\delta_2$ only depends on $2\pi f\delta_2/u_e$ and velocity profile shape factor.
- 4) At separation, the dividing streamline is straight, forming an angle γ with the airfoil surface.

It should be noted that the first two assumptions are quite contradictory to previous discussion. However, it is believed that the errors they introduce can be corrected by some minor adjustments on the value of n_7 , which is input by the user.

With assumption 4, Van Ingen suggests the following correlation:

$$\tan(\gamma) = \frac{B}{Re_{\delta_2, s}} \quad (60)$$

where B is found experimentally to range between 15 and 20. Van Ingen thus assigns a universal value of 17.5 to B . Schmidt [46] also provides a newer correlation which is tailored for low Re_c conditions when bubble is dominating. It states that,

$$B = 2.7034 + 2149.1 \Lambda_{2s}^2 \quad (61)$$

where Λ_2 , the Pohlhausen parameter, has been defined in Eq. (28). As Schmidt explains, B ranges from 12.6 to 23.8 if typical Λ_{2s} values ($-0.099 < \Lambda_{2s} < -0.068$) is substituted in Eq. (61). This agrees well with Van Ingen's findings. However, preliminary testing suggested that the value of B is very sensitive to Λ_{2s} , which can change considerably with a small shift in the separation location. Therefore, the current project continues to use 17.5 as a constant value of B because of its reliability.

Van Ingen then introduces a new transformed bubble laminar length, z , which is defined as,

$$\begin{aligned}
z &= |B \xi \Lambda_{2S}| \\
&= B \left[\frac{l_1}{\delta_{2S} Re_{\delta_{2,S}}} \right] \left[-\frac{\delta_{2S}^2 \left(\frac{du_e}{ds} \right)_S}{\nu} \right]
\end{aligned} \tag{62}$$

Thus, using assumption 1 and Eq. (62), the integral in Eq. (59) can be expressed as,

$$\begin{aligned}
&\int -\alpha_i ds \\
&= Re_{\delta_{2,S}} \int \frac{-\alpha_i \delta_2}{(\delta_2 / \delta_{2S})} d\xi \\
&= (10^{-4}) \frac{Re_{\delta_{2,S}}}{B \Lambda_{2S}} \left[10^4 \int (-\alpha_i \delta_2) dz \right]
\end{aligned} \tag{63}$$

With I defined by,

$$I = \max \left[(10^4) \int_{z_s}^z (-\alpha_i \delta_2) dz \right] \tag{64}$$

Eq. (59) and Eq. (63) can be combined to form:

$$\begin{aligned}
n_{ST} &= (10^{-4}) \frac{Re_{\delta_{2,S}}}{B \Lambda_{2S}} \max \left[(10^4) \int_{z_s}^z (-\alpha_i \delta_2) dz \right] \\
&= (10^{-4}) \frac{Re_{\delta_{2,S}}}{B \Lambda_{2S}} I
\end{aligned} \tag{65}$$

where n_{ST} designates the amplification between separation and transition.

Applying linear stability theory with spatial growth, and using assumptions 2 and 3, the integral in Eq. (65) can be evaluated for various f 's as a function of z and the values can be represented by the solid lines in Figure 20. Consequently, $I(z)$ is represented by the dashed line, which envelops all these solid curves. After organizing

all these numerically generated data, Van Ingen is able to express I as a fairly simple function of z :

$$I = \begin{cases} 122.5 + 530z & z \leq 0.9877 \\ 650\sqrt{z} & z > 0.9877 \end{cases} \quad (66)$$

For application, I is first calculated by substituting n_{ST} and other separation parameters into Eq. (65). Then z can be obtained by inverting Eq. (66). Finally I can be calculated according to Eq. (62). These equations will replace Eq. (41) as the transition criterion in the current project. The only problem left is to find a suitable value for n_{ST} . According to assumption 2 which states that the amplification of TS waves before separation is negligible, n_{ST} should be equal to the input value of n_T . However, preliminary program testing shows that substituting n_T directly into Eq. (65) can over-predict the bubble length if n_s , the accumulated TS waves growth at separation point, is close to n_T . Thus, to ensure that a unified parameter, n_T , can be applied to both attached and separated flow, the following empirical correlations are used in the current project:

$$n_{T,\min} = \max(10, 0.75n_T)$$

$$Rt = n_s / n_T$$

$$n_{ST} = \begin{cases} n_T & Rt < 0.5 \\ n_T - \left[\frac{Rt - 0.5}{0.3} (n_T - n_{T,\min}) \right] & 0.5 < Rt < 0.8 \\ n_{T,\min} & 0.8 < Rt \end{cases} \quad (67)$$

Eq. (67) is also illustrated in Figure 21 for clarification.

The use of $n_{T,\min}$ in Eq. (67) is to put a limit on the minimum length of the bubble, so that the prediction will not show unrealistic drag reduction. Although the correlations in Eq. (67) seem arbitrary, using them gives better agreement with experimental data than assuming negligible TS waves growth prior to separation. The

correlations also suggest that the amplifications in separated flow dominate over those in attached flow. This agrees with the fact that laminar separated flow is highly unstable compared to laminar attached flow.

After determining l_1 and hence the transition location, the laminar shear layer growth can be expressed as a function of the separation condition by integrating the boundary layer equations between S and T . For instance, using Eq. (15) and the Stewartson profiles, Van Ingen et al. [25] obtain the following:

$$\bar{\delta}_2 = \frac{\delta_2}{\delta_{2S}} = \begin{cases} \{1 + 0.152[1 - (1 - 0.75\xi)^4]\}^{1.25} & 0 \leq \xi \leq 1.3333 \\ 1.1935 & \xi > 1.3333 \end{cases} \quad (68)$$

with the transformed streamwise coordinate ξ already defined in Eq. (38).

On the other hand, Schmidt [46] argues that the separated shear layer on an airfoil surface bears a strong resemblance to the free shear layer in terms of pressure gradient and velocity profile similarity. Therefore, by drawing analogy to the theoretical δ_2 growth in a free shear layer and using ξ as a fundamental scale in laminar flow, Schmidt suggests that,

$$\bar{\delta}_2 = \sqrt{1 + (1.241)^2 \xi} \quad (69)$$

He also points out that Eq. (69) predicts substantially more growth than Eq. (68). Eq. (69) will be used in the current project because it agrees better with experimental results, specially in low Re_c conditions when bubble becomes a dominating feature on an airfoil [46].

3.4 Modifications on Turbulent Region and Reattachment Modelling

As discussed in section 3.2, the turbulent separated flow model in Horton's method is solely based on Eq's. (15) and (16), which represent the direct mode of boundary layer calculation. However, Dini [33] finds that calculation of separated flow using direct mode is very sensitive even to the smallest variations in the input u_e ,

distribution. He suggests that the inverse mode of the boundary layer equation should be used and he cites two equations derived by Eppler as an example:

$$\frac{du_e}{ds} = \left[\frac{C_f H_{32}}{2} - C_d + \delta_2 \frac{dH_{32}}{ds} \right] \frac{u_e}{\delta_2 H_{32} (H_{12} - 1)} \quad (70)$$

$$\frac{d\delta_2}{ds} = \left[-\frac{3C_f H_{32}}{2(H_{12} + 2)} + C_d - \delta_2 \frac{dH_{32}}{ds} \right] \frac{H_{12} + 2}{H_{32} (H_{12} - 1)} \quad (71)$$

The major difference between the direct mode and the inverse mode lies in the use of the u_e distribution. It can be seen that u_e is used as an input in Eq's. (15) and (16), while it is generated as an unknown in Eq. (70). As well as being used in the calculation of separated flow, boundary layer equations in inverse mode can of course be used to generate the u_e distribution for optimum pressure recovery. Classic examples include the Stratford's [8], [9] recovery and the Wortmann's [12] recovery, which have been discussed in Chapter 1.

Following Drela and Giles [32], Dini [33] uses three integral equations to calculate the growth of the turbulent shear layer. They include Eq's. (70) and (71), which are in the inverse mode. The other one is Eq. (21), which is required to account for the non-equilibrium in the flow due to the response lag to the rapidly changing pressure gradient. To have the calculation proceed, Dini has to prescribe the H_{32} distribution, with the continuity of its curvature maintained from the transition location to the overshoot region downstream of reattachment. However, one of the parameters in the H_{32} distribution is left as an unknown. Its value is determined through an internal iteration loop which runs on until the generated u_e distribution can merge with the inviscid u_e distribution smoothly. Reattachment is assumed to occur at the point where Horton's [45] reattachment criterion, Eq. (53), is satisfied.

The closure to the three equations, Eq.'s (70), (71), and (21), is completed with Drela et al.'s correlations between C_d , H_{12} , C_f , and $C_{r,EQ}$. Since the correlations are developed for the trailing edge turbulent separation with less recirculation and

entrainment, Dini has to modify the correlations to reflect the higher values of C_d and C_f typical to the turbulent part of the bubble.

Due to Dini's observation, the turbulent shear layer model in Horton's method should be replaced by one which is based on the inverse mode boundary layer equations. Inevitably, the analysis program will become more complicated and less efficient if the boundary layer calculation has to switch between direct and inverse modes. Therefore, it is preferred to have an analytical relationship which can express the reattachment condition in terms of the transition condition.

In view of Van Ingen et al.'s [25] successful application of Stratford's recovery as bursting criterion, it was decided to adopt the similar but more flexible Wortmann's recovery to model the turbulent shear layer in the current project. Although Wortmann's recovery was originally developed for attached flow on the verge of separation, it is likely that it is applicable to the turbulent region development with little error due to the shortness of the region. Nevertheless, the concave u_e distribution resulting from Wortmann's recovery certainly agrees better with experimental observation than the linear u_e distribution proposed by Horton.

With the consideration that growth in the laminar region is substantial, variables will be normalized using transition condition (δ_{2T}, u_{eT}) , rather than using separation condition as done by Horton. To avoid confusion, the overcap, $\hat{\cdot}$, will be used from this point on to represent variables normalized against transition condition. For example, \hat{u}_e represents u_e/u_{eT} .

With the new notation, the u_e distribution generated from Wortmann's [12] recovery can be expressed as,

$$\hat{u}_e = \frac{u_e}{u_{eT}} = [1 + \beta(\hat{s} - \hat{s}_T)]^{-m} \quad (72)$$

where

$$m = 0.33 - \frac{0.074}{6 \beta Re_c^{0.2}} \quad (73)$$

Kennedy [11] suggests that a u_c distribution with the value of H_{l_2} staying at 1.8 required $\beta = 9.2(10^{-3})$ at $Re_c = 10^6$, and $\beta = 8.0(10^{-3})$ at $Re_c = 5(10^6)$. Since these values are derived for attached flow on the verge of separation, it is expected that some adjustments within the same order of magnitude are necessary before they can be applied to the bubble turbulent region.

At reattachment, Eq. (72) can be rewritten as,

$$\hat{u}_{eR} = \frac{u_{eR}}{u_{eT}} = [1 + \beta \hat{l}_2]^{-m} \quad (74)$$

Now, Eq. (74) can be coupled with the u_c distribution generated from potential flow calculation to solve for u_{eR} and l_2 . Thus, Eq. (74) replaces Eq. (50) as the iterative mechanism. Likewise, bursting is assumed to occur if the iterative scheme fails to produce converged values of u_{eR} and l_2 . Preliminary testing suggests that Eq. (74) is more successful in predicting bursting than Eq. (50), as Eq. (50) fails to predict the occurrence of reattachment in some cases. The better performance of Wortmann's concave u_c distribution is due to its allowing more overall deceleration in the bubble region ($u_{eR} - u_{eS}$) than Horton's linear distribution, with the same reattachment velocity gradient $(du_c/ds)_R$ in both cases. Van Ingen et al. [25] observe the same trend when using the also concave Stratford u_c distribution. In addition, being a much simpler formulation with variables in lower order, Eq. (74) takes fewer iterations to achieve convergence, thus saving computation time. These are the two reasons why Eq. (74) was used in the current project.

Following Horton, Eq. (46) was used to calculate the growth of the turbulent shear layer. Integrating it between T and R and representing H_{f2} , C_d with some overall mean values results in:

$$\delta_{2R} u_{eR}^3 - \delta_{2T} u_{eT}^3 = \frac{C_{dm}}{H_{32m}} \int_{s_T}^{s_R} u_e^3 ds \quad (75)$$

With the new notation, Eq. (75) can be normalized to form,

$$\hat{\delta}_{2R} \hat{u}_{eR}^3 - 1 = \frac{C_{dm}}{H_{32m}} \int_{\hat{s}_T}^{\hat{s}_R} \hat{u}_e^3 d\hat{s} \quad (76)$$

Readers can note the similarity between Eq. (76) and Eq. (47) developed by Horton. Now, Eq. (72) can be substituted into Eq. (76). After evaluating the integral, the following is obtained:

$$\hat{\delta}_{2R} \hat{u}_{eR}^3 - 1 = \frac{C_{dm}}{H_{32m}} \left[\frac{(1 + \beta \hat{l}_2)^{(-3m+1)} - 1}{\beta (-3m + 1)} \right] \quad (77)$$

With some transformation, the growth of the turbulent region can be expressed as,

$$\frac{\delta_{2R}}{\delta_{2T}} = \hat{\delta}_{2R} = \frac{1}{\hat{u}_{eR}^3} \left\{ 1 + \frac{C_{dm}}{H_{32m}} \left[\frac{(1 + \beta \hat{l}_2)^{(-3m+1)} - 1}{\beta (-3m + 1)} \right] \right\} \quad (78)$$

Both u_{eR} and l_2 in Eq. (78) have been determined through the iterative scheme, leaving C_{dm} and H_{32m} as the only unknowns. Horton suggests that $C_{dm} = 0.0182$, but Roberts [48] argues that Horton obtains the value in a condition that the velocity gradient is zero. Therefore, he suggests a much higher value of C_{dm} at 0.0350, which can account for the larger flow dissipation associated with the steep velocity gradient typical to the turbulent region. This is also supported by Schmidt [46] who states that prediction of δ_2 can be more accurate using Robert's value for C_{dm} . However, numerical expressions from Drela et. al. [32] and Dini [33] suggests that C_{dm} can vary considerably with Re_c . In fact, it is the main object of the current project to determine the value of C_{dm} at various conditions characterized by combinations of Re_c and n_T . On the other hand, there

seems to be no objection to Horton's suggestion that $H_{32m} = 1.50$, so the same value was used in the current project.

It may have been noticed that the parameter Λ_R is no longer involved in the calculation after the introduction of Wortmann's u_e distribution, but its value can still be evaluated. First, the velocity gradient of Wortmann's distribution can be expressed as,

$$\frac{d\hat{u}_e}{d\hat{s}} = -m\beta [1 + \beta(\hat{s} - \hat{s}_T)]^{-(m+1)} \quad (79)$$

which can then be substituted into the definition of Λ in Eq. (45) and the following can be obtained:

$$\Lambda_R = \frac{\delta_{2R}}{\hat{u}_{eR}} \left(\frac{d\hat{u}_e}{d\hat{s}} \right)_R = \frac{\delta_{2R}}{\hat{u}_{eR}} \left[\frac{-m\beta}{(1 + \beta\hat{l}_2)^{(m+1)}} \right] \quad (80)$$

The calculated value of Λ_R can be used in checking the validity of the bubble model, as Schmidt [46] suggests that Λ_R should range between -0.0099 and -0.0060 based on experimental results from O'Meara. Thus this provides a guideline for obtaining the value of β in Eq. (74).

It is not known whether the error due to the use of mean values like C_{dm} and H_{32m} is small enough so that it will not jeopardize the airfoil C_D prediction, but the bubble model can be verified by testing it against the experimental data of various airfoils collected in a wide range of conditions. This can be done simultaneously when investigating the dependence of β and C_{dm} on Re_c and n_T . The findings and the verifications are documented in Chapter 4.

Chapter 4 Calibration and Verification

Since the two parameters, β and C_{dm} , are left open in the bubble model, it is necessary to calibrate them with experimental data on a trial and error basis. Then the validity of the bubble model can be verified by applying it to other airfoils. To increase the credibility of the current project, the airfoils selected for calibration and verification are of various aerodynamicists' designs and the experimental data are from several different wind tunnels. The calibration will be discussed in section 4.1, while the verification will be discussed in section 4.2.

4.1 Calibration

The airfoils selected for calibration include Eppler 387, FX 66-17A-175, and FX 66-S-196 V1 [44] (see Figure 22). The first two have been discussed in section 2.3 with their shapes shown in Figure 8 and Figure 9 respectively. The FX 66-S-196 V1 airfoil is selected because its data is available at $Re_c = 0.5(10^6)$, so the gap ($0.3(10^6) < Re_c < 10^6$) left by the first two sets of data can be filled. It should be noted that the calibration is limited in the Re_c range between $0.2(10^6)$ and $1.5(10^6)$. With Re_c higher than $1.5(10^6)$, the effect of the bubble is so small that reliable data is not available for calibration. On the other hand, if Re_c drops below $0.2(10^6)$, the bubble generally extends to have substantial perturbation on the u_c distribution outside the bubble region. Reliable results using the current bubble model are not expected for such low Re_c . As mentioned in Chapter 2, the value of n_T can vary from 10 (wind tunnel) to 15 (free-flight) according to freestream turbulence level Tu .

The calculated results of the Eppler 387 airfoil at $Re_c = 0.2(10^6)$ and $0.3(10^6)$ using the modified codes are shown in Figure 23 and Figure 24 respectively. The value of n_T was chosen to be 11.2. The reason for choosing β as 0.022 is that it gives the closest agreement between the calculated and the measured bubble length, l , especially at $Re_c = 0.3(10^6)$. This value of β is several times larger than that supplied by

Wortmann, suggesting that the bubble region has a higher boundary layer growth rate than attached flow. As shown in Table 1 ($Re_c = 0.2(10^6)$) and Table 2 ($Re_c = 0.3(10^6)$), the relative difference between the predicted and the measured l are within 20% at a wide range of α . The agreement at $Re_c = 0.3(10^6)$ can be described as excellent, while the agreement at $Re_c = 0.2(10^6)$ is relatively inferior. However, it is speculated that the disagreement is due to the over-prediction of l_1 , which is not related to the value of β . In fact, the over-prediction of l_1 at $Re_c = 0.1(10^6)$ is confirmed by comparison with experimental data [43]. Also, choosing β as 0.022 produces Λ_R values which are within the range suggested by Schmidt [46]. This topic will be discussed in more detail in section 4.2.

With β fixed at 0.022, the optimal value of C_{dm} can then be found on a trial and error basis. After some iterations, the value of C_{dm} is chosen to be 0.017 at $Re_c = 0.2(10^6)$ and 0.025 at $Re_c = 0.3(10^6)$. As seen in Figure 24, the agreement of the predicted and the measured drag polar is excellent at $Re_c = 0.3(10^6)$. The agreement at $Re_c = 0.2(10^6)$ (Figure 23) deteriorates slightly, most likely due to the over-prediction of l_1 . Nevertheless, the accuracies of the prediction in both cases are improved after the addition of the bubble model.

The results of the FX 66-17A-175 airfoil at $Re_c = 10^6$ and $1.5(10^6)$ using the modified codes are shown in Figure 25 and Figure 26 respectively. The value of n_T was chosen to be 14. Again, based on the output Λ_R values, β is chosen to be 0.022. The optimal values of C_{dm} is found to be 0.055 at $Re_c = 10^6$ and 0.075 at $Re_c = 1.5(10^6)$. Figure 25 and Figure 26 show that excellent results can be obtained with such combinations of β and C_{dm} at the respective Re_c . The only exception is at the C_L range between 0.25 and 0.55, where C_D is under-predicted by a maximum of 0.0007 at $Re_c = 10^6$ and by a maximum of 0.001 at $Re_c = 1.5(10^6)$. After reviewing the boundary layer development, it is speculated that the drastic drag increase at that C_L range is caused by a bubble located near the leading edge on the lower surface. This illustrates that the bubble model is more accurate in predicting mid-chord bubbles than leading edge

bubbles. It is probably due to the much larger velocity gradient, $(du_x/ds)_s$, encountered by leading edge bubbles.

The experimental data for the FX 66-S-196 V1 airfoil at $Re_c = 0.5(10^6)$ are obtained from Horstmann et. al. [19]. Since the airfoil was tested in the Low Speed Laboratory at Delft University of Technology (Delft LSL), the value of n_T was chosen to be 11.2 following Van Ingen et. al. [25]. Figure 27 shows that excellent results can be obtained by choosing β as 0.022, and C_{dm} as 0.035 at $Re_c = 0.5(10^6)$.

After calibrating the bubble model with the above three sets of data, it is proposed that β has a universal value of 0.022 at all combinations of n_T and Re_c , while C_{dm} is dependent on Re_c only. As shown in Figure 28, the correlations between C_{dm} and Re_c can be determined by fitting a cubic spline through the above findings, which suggest that $C_{dm} = 0.017, 0.025, 0.035, 0.055, \text{ and } 0.075$ at $Re_c = 0.2(10^6), 0.3(10^6), 0.5(10^6), 10^6,$ and $1.5(10^6)$ respectively.

4.2 Verification

The airfoils selected for verification include Eppler 387 (at $Re_c = 0.46(10^6)$), FX 61-163 ([44], Figure 29), Eppler 403 ([10], Figure 30), FX S02/1-158 ([44], Figure 31), UAG 88-143/20 ([2], Figure 32), and FX LV-152 ([44], Figure 33). The bubbles on the first two airfoils are so small that they are close to being eliminated, while the bubbles on the other four airfoils are dominant and definitely increase the airfoil drag. Thus, by testing against these six airfoils, the effectiveness of the bubble model at a wide range of bubble dominance can be illustrated.

Figure 34 shows the results for the Eppler 387 airfoil at $Re_c = 0.46(10^6)$. It can be seen that the bubble model codes over-predict C_D slightly (by about 0.0003) because the bubble is relatively small at this design Re_c . Nevertheless, the results from the modified codes are accurate enough for engineering purposes. Also, by comparing the results generated with and without the bubble model, the user can appreciate that the drag increase due to the bubble is negligible.

The experimental data of the FX 61-163 airfoil are obtained from Boermans and Selen [51]. Since the airfoil was tested at Delft LSL, n_T was chosen to be 11.2. Figure 35 and Figure 36 show the results at $Re_c = 10^6$ and $1.5(10^6)$ respectively. It can be seen that the bubble model gave excellent prediction in both cases. The only disagreement is located at the C_L range near stall, but this is due to inaccurate prediction of the turbulent separation location. These two cases again illustrate that the bubble model can produce reliable predictions even if the bubble size is small.

The Eppler 403 airfoil was tested at $Re_c = 10^6$ in Stuttgart LWT [10], so n_T was chosen as 14. As seen in Figure 37, major improvement in predicting the drag polar is obtained after the addition of the bubble model, although C_D is still under-predicted by about 0.0008 at $C_L = 0.2$. The under-prediction is probably due to excessive bubble size (12% c at $Re_c = 10^6$).

The results for the FX S02/1-158 airfoil at $Re_c = 10^6$ and $1.5(10^6)$ are shown in Figure 38 and Figure 39 respectively. n_T was chosen as 14 because the airfoil was tested at Stuttgart LWT. It can be seen that there is improvement in predicting the drag polar in both cases after the addition of the bubble model, although it is not as large as the improvement for the Eppler 403 case.

The UAG 88-143/20 airfoil might be the most challenging one of the selected six to simulate. To reduce drag, the airfoil is designed to have its pressure recovery at about 60% chord. Thus, the velocity gradient at separation is relatively high, resulting in large separation bubble. Again, n_T was chosen as 14 because the airfoil was tested at Stuttgart LWT [52]. It can be seen in Figure 40 that the bubble model brings major improvement to the drag prediction at $Re_c = 0.7(10^6)$ when the bubble length can extend to about 10% chord. The improvements at $Re_c = 10^6$ (Figure 41) and at $1.5(10^6)$ (Figure 42) are smaller, illustrating that the bubble dominance decreases with higher Re_c .

The final airfoil to be verified against is FX LV-152, which is symmetric in shape. Figure 43 shows that dramatic improvement is obtained at $Re_c = 0.5(10^6)$ after the addition of the bubble model, although C_D is still under-predicted by 0.001 at $C_L = 0.35$. The calculation shows that at $C_L = 0.35$, the length of the upper surface bubble

is 14% chord, while the bubble on the lower surface has its length extended to 21% chord. It is likely that the excessive bubble size on the lower surface causes the under-prediction.

As mentioned in Chapter 3, the theoretical value of Λ_R calculated from Eq. (80) can be used to check the validity of the bubble model. Table 3 shows the calculated Λ_R ranges for various airfoils with β set at 0.022. These data are gathered from mid-chord bubbles only, but cover a wide range of bubble size and Re_c . Except for two cases in which the minimum Λ_R values are slightly out of range, all the other cases have Λ_R values well within the suggested range ($-0.0060 > \Lambda_R > -0.0099$) from Schmidt [46]. Therefore, 0.022 should be an appropriate value for β .

Finally, the sensitivity of the drag prediction towards the values of C_{dm} and β should be investigated. Two test cases are selected, which include Eppler 387 at $Re_c = 0.3(10^6)$, UAG 88-143/20 at $Re_c = 10^6$. Both airfoils have bubbles of more than 10% chord long. Figure 44 shows the effect of changing C_{dm} on the C_D prediction of the Eppler 387 airfoil at $Re_c = 0.3(10^6)$. Increasing C_{dm} from 0.025 to 0.035 increases the C_D prediction by an average of 0.0006, while reducing C_{dm} to 0.015 causes the C_D prediction drop by an average of 0.0004. Figure 45 shows the effect of C_{dm} on the C_D prediction of the UAG 88-143/20 airfoil at higher Re_c . At $Re_c = 10^6$, changing C_{dm} by 0.01 affects the C_D prediction by less than 0.0002. Figure 46 shows the effect of β on the C_D prediction of the Eppler 387 airfoil at $Re_c = 0.3(10^6)$. Increasing β from 0.022 to 0.030 reduces the C_D prediction by an average of 0.0002, while reducing β to 0.015 causes the C_D prediction increase by an average of 0.0006. Similar trend can be observed in Figure 47 which shows the effect of β on the C_D prediction of the UAG 88-143/20 airfoil at $Re_c = 10^6$. Increasing β from 0.022 to 0.030 reduces the C_D prediction by an average of 0.0002, while reducing β to 0.015 causes the C_D prediction increase by an average of 0.0009. Thus, it is concluded that airfoil C_D prediction is fairly sensitive to the values of C_{dm} and β , so careful calibration of the bubble model is necessary.

The test cases from these six airfoils suggest that the bubble model can indeed improve the drag prediction, especially when it is applied to the mid-chord bubble. The

bubble model can be applied to a leading edge bubble, but the prediction accuracy needs some improvement. Also, some improvements must be made on the calculation of l , before the bubble model can be applied to situations with Re_c less than $0.2(10^6)$.

Chapter 5 Conclusion

In the current project, a separation bubble model was developed and incorporated into an existing airfoil analysis program to improve its drag prediction accuracy at low Re_c . To be retro-fitted to the boundary layer calculation in the original program, the bubble model was based on boundary layer integral equations. Also, a minimum amount of additional computation tasks were added to the original program, while producing results accurate for engineering purposes. Based on these requirements, Horton's method was chosen for the current project. However, after some preliminary testing, it was found that Horton's original bubble model seriously under-predicts bubble growth and results in inaccurate C_D prediction.

To improve the model, the original formulations had to be replaced with those which agree more closely with experimental observations on bubbles. Therefore, Van Ingen's and Schmidt's correlations were adopted for the calculation of the laminar region of the bubble, so that both the effect of freestream turbulence on transition and the substantial boundary layer growth in the laminar region could be accounted for. On the other hand, the linear velocity distribution proposed by Horton was replaced by the concave velocity distribution resulting from Wortmann's optimum pressure recovery to produce a better simulation of the turbulent region of the bubble. Table 4 contains a comparison of the original and modified Horton's bubble model for references.

Calculation using the bubble model can start after the laminar separation location is determined by viscous-inviscid interaction. Besides functioning as a link between the laminar and turbulent boundary layers, the bubble model also acts as a bursting criterion. Testing with six sets of experimental data from various wind tunnels confirms that the bubble model can simulate mid-chord bubbles in the Re_c range between $0.2(10^6)$ and $1.5(10^6)$ with accuracy good enough for engineering purposes. The model can be applied to leading edge bubbles, but the accuracy still requires improvement, due to the extremely adverse u_x gradient usually encountered by leading edge bubbles. Compared with other bubble models, the current one is probably the simplest available. This is because the calculation only involves parameters at three locations (separation, transition,

and reattachment), thus avoiding the need of numerical integration between these points. Its simplicity allows the current bubble model to be used in airfoil analysis even on desktop computers. Otherwise, it is also a convenient means to obtain initial values for more advanced forms of calculation.

Finally, there are some suggestions on how the current bubble model can be further improved. Firstly, newer correlations should be used to calculate l_i before the model applicable Re_c range can be extended to below $0.2(10^6)$. This also improves the prediction accuracy when the bubble being simulated is close to disappearance. Secondly, the correlations between C_{dm} and Re_c should be extended to beyond the Re_c range between $0.2(10^6)$ and $1.5(10^6)$ with a broader data base because bubble appearance is certainly not limited to the above range. Thirdly, the bubble model should be incorporated as part of the viscous-inviscid interaction, rather than as an addendum to the interaction as in the current project. However, this can only be done with some numerical smoothing on the δ_i distribution generated from the boundary layer calculation. Otherwise, local perturbations on the u_x distribution due to the rapid δ_i change in the bubble will cause serious instabilities in determining the separation location.

Tables**Table 1** Comparison of measured and calculated separation location, bubble size on the upper surface for the Eppler 387 airfoil at $Re_c \approx 0.2(10^6)$

α , deg.	x_s		l	
	meas.	calc.	meas.	calc.
-2	0.53	0.52	0.27	0.34
0	0.48	0.47	0.26	0.34
2	0.43	0.43	0.24	0.29
4	0.40	0.38	0.22	0.23
5	0.38	0.34	0.21	0.18
7	0.33	0.29	0.15	0.17

Table 2 Comparison of measured and calculated separation location, bubble size on the upper surface for the Eppler 387 airfoil at $Re_c = 0.3(10^6)$

α , deg.	x_s		l	
	meas.	calc.	meas.	calc.
-2	0.53	0.52	0.21	0.21
0	0.48	0.47	0.21	0.20
2	0.45	0.44	0.17	0.18
4	0.40	0.38	0.18	0.14
5	0.39	0.34	0.16	0.13
6	0.38	0.35	0.12	0.15

Table 3 Calculated Λ_R ranges for various airfoils with $\beta = 0.022$

Airfoil and [data source]	Re_c /10 ⁶	C_{dm}	Λ_R range:			
			max. Λ_R @ (l)		min. Λ_R @ (l)	
Eppler 387 [N]	0.2	0.017	-0.0069	(0.18)	-0.0074	(0.34)
	0.3	0.025	-0.0071	(0.12)	-0.0076	(0.20)
	0.46	0.030	-0.0074	(0.10)	-0.0076	(0.12)
FX 66-S-196 V1 [D]	0.5	0.035	-0.0075	(0.06)	-0.0090	(0.13)
FX 66-17A-175 [S]	1.0	0.055	-0.0081	(0.05)	-0.0088	(0.07)
	1.5	0.075	-0.0081	(0.04)	-0.0086	(0.05)
FX 61-163 [D]	1.0	0.055	-0.0072	(0.04)	-0.0079	(0.06)
	1.5	0.075	-0.0076	(0.04)	-0.0079	(0.04)
Eppler 403 [S]	1.0	0.055	-0.0069	(0.05)	-0.0102*	(0.12)
FX S02/1-158 [S]	1.0	0.055	-0.0078	(0.05)	-0.0089	(0.08)
	1.5	0.075	-0.0080	(0.04)	-0.0090	(0.06)
UAG 88-143/20 [S]	0.69	0.043	-0.0071	(0.07)	-0.0106*	(0.15)
	1.0	0.055	-0.0072	(0.05)	-0.0098	(0.10)
	1.5	0.075	-0.0072	(0.04)	-0.0089	(0.07)
FX LV-152 [S]	0.5	0.035	-0.0071	(0.08)	-0.0089	(0.21)

Legend:N - NASA Langley Low-Turbulence Pressure Tunnel, $n_T = 11.2$ D - Low Speed Laboratory of the Delft University of Technology, $n_T = 11.2$ S - Laminar Wind Tunnel at University of Stuttgart, $n_T = 14$ * - out of suggested range ($-0.0060 > \Lambda_R > -0.0099$)

Table 4 Comparison of original and modified Horton's method

parameter	original formulations	modified formulations
u_{eT}	Eq. (39)	Eq's (37) and (38)
l_1	Eq. (41)	Eq's (62) - (67) with $B = 17.5$
δ_{2T}	Eq. (39)	Eq. (69)
C_{dm}	0.035	$C_{dm}(Re_c)$, Figure 28
H_{32m}	1.50	1.50
Λ_R	-0.0082	Eq. (80)
β	N / A	0.022
m	N / A	Eq. (73)
u_{eR}	Eq. (50) and airfoil u_e distribution from panel method	Eq. (74) and airfoil u_e distribution from panel method
l_2		
δ_{2R}	Eq. (55)	Eq. (78)
H_{32R}	1.51	1.51

Figures

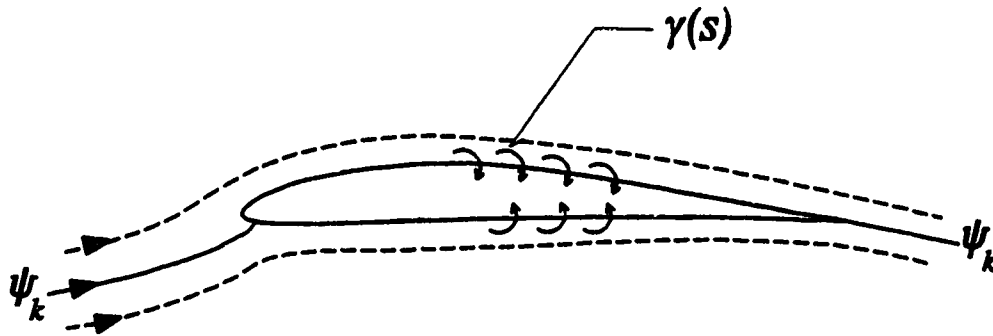


Figure 1 Vortex representation of a single component airfoil

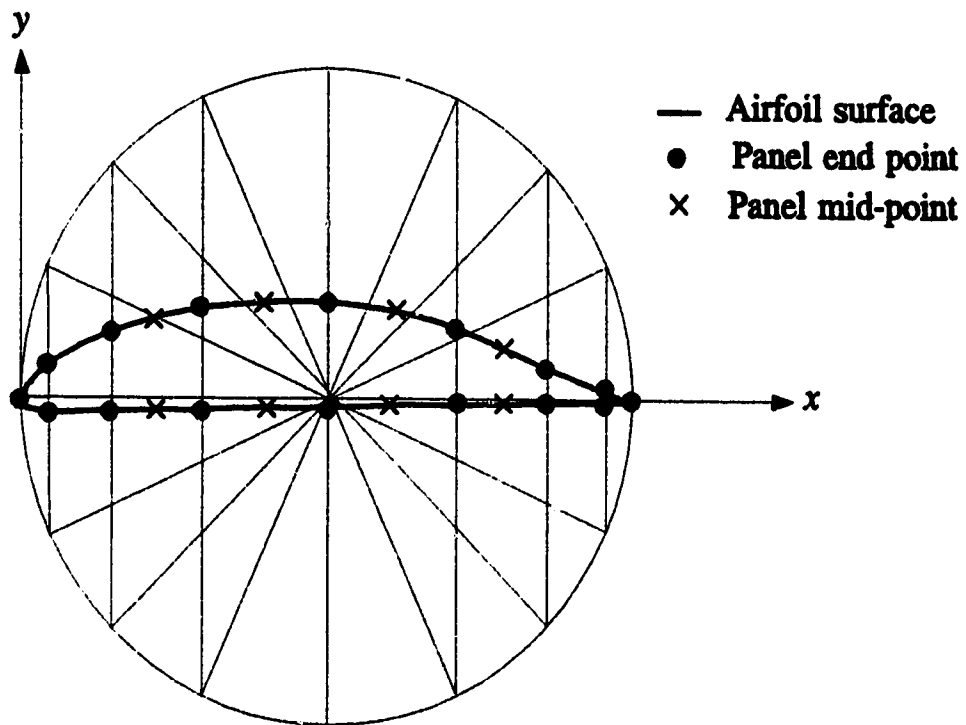


Figure 2 Locations of panels on airfoil surface

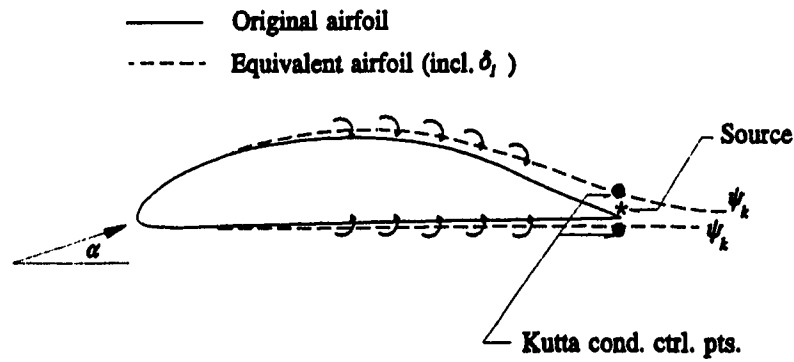


Figure 3 Simulating equivalent airfoil with a trailing edge source

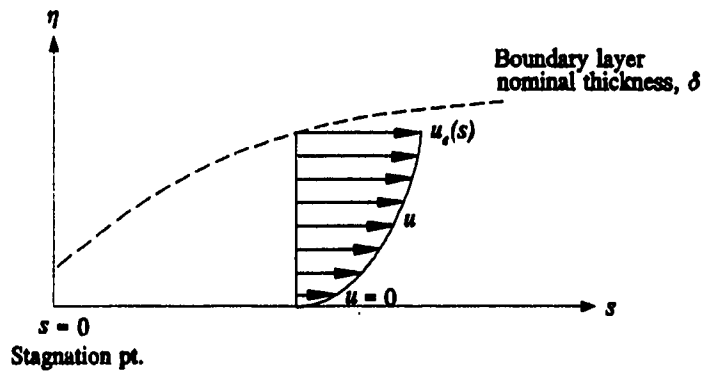


Figure 4 Typical velocity profile in boundary layer

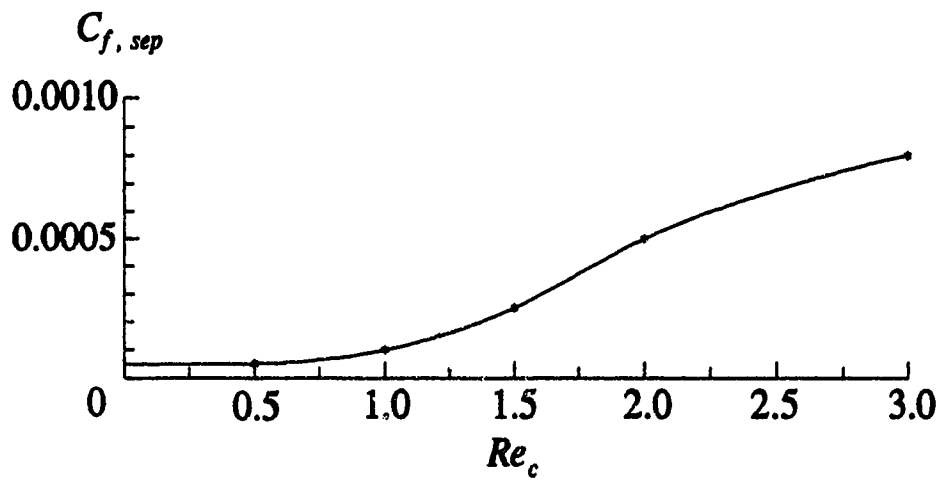


Figure 5 Correlations between $C_{f, sep}$ and Re_c

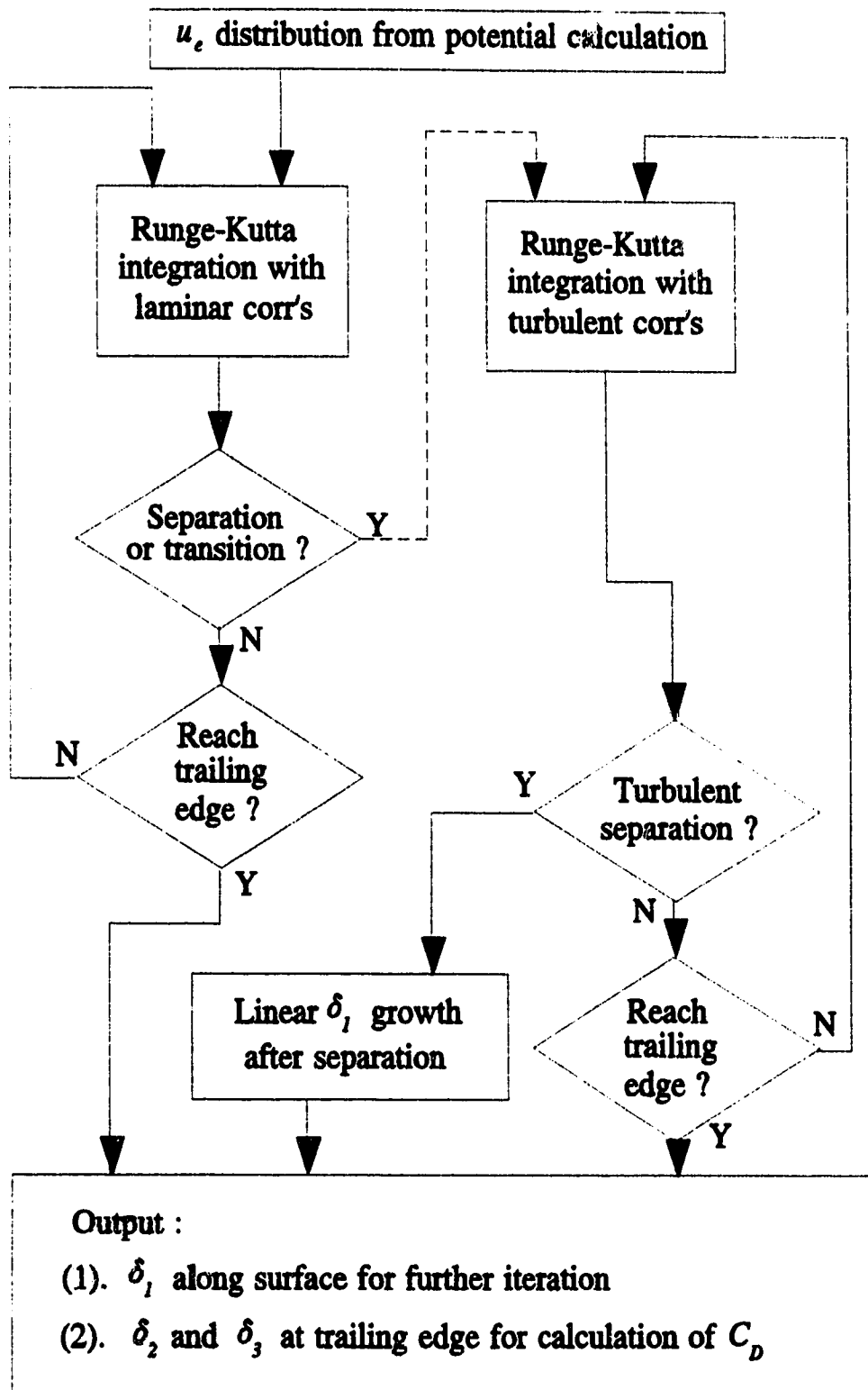


Figure 6 Boundary layer calculation flow chart

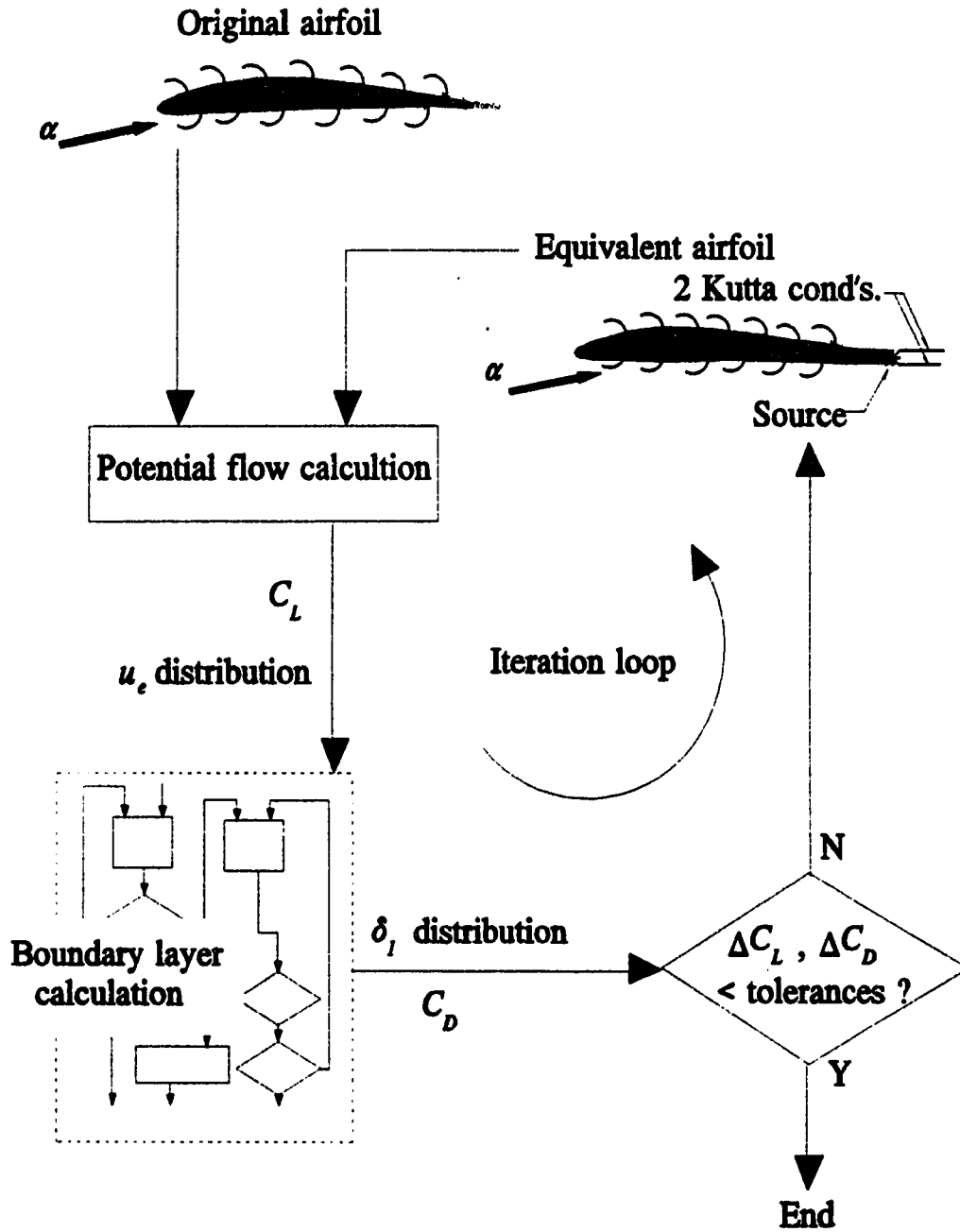


Figure 7 Viscous-inviscid interaction

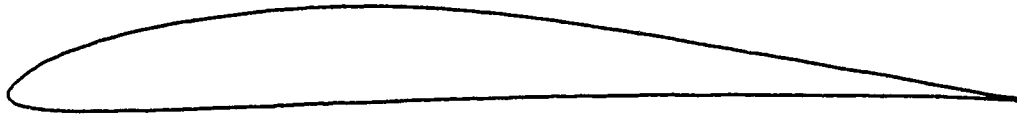


Figure 8 Eppler 387 airfoil

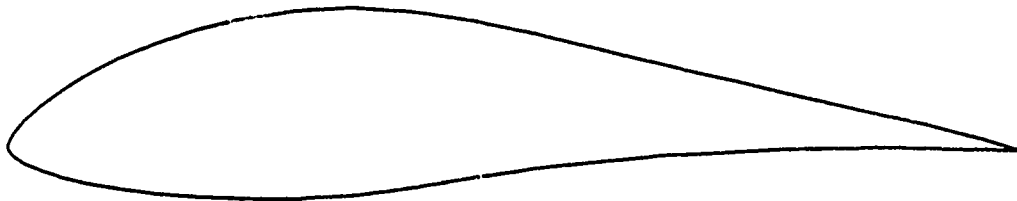


Figure 9 FX 66-17A-175 airfoil

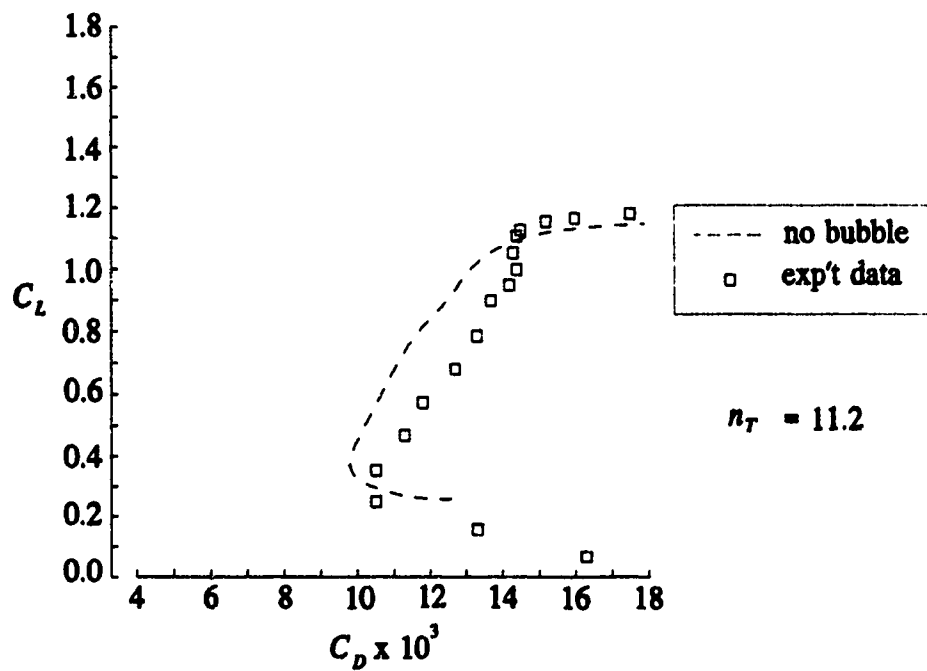


Figure 10 Eppler 387 airfoil at $Re_c = 0.2(10^6)$

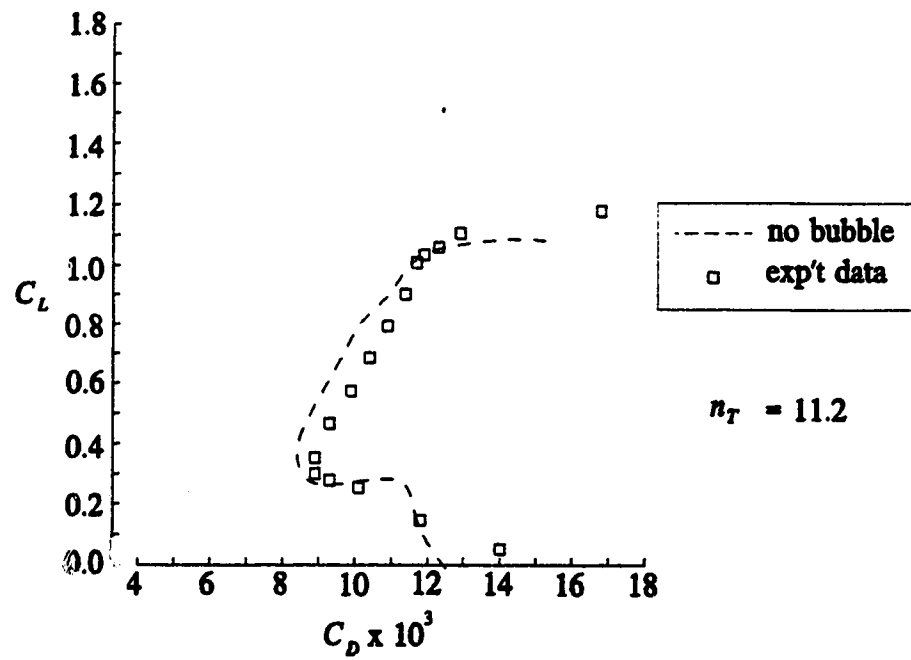


Figure 11 Eppler 387 airfoil at $Re_c = 0.3(10^6)$

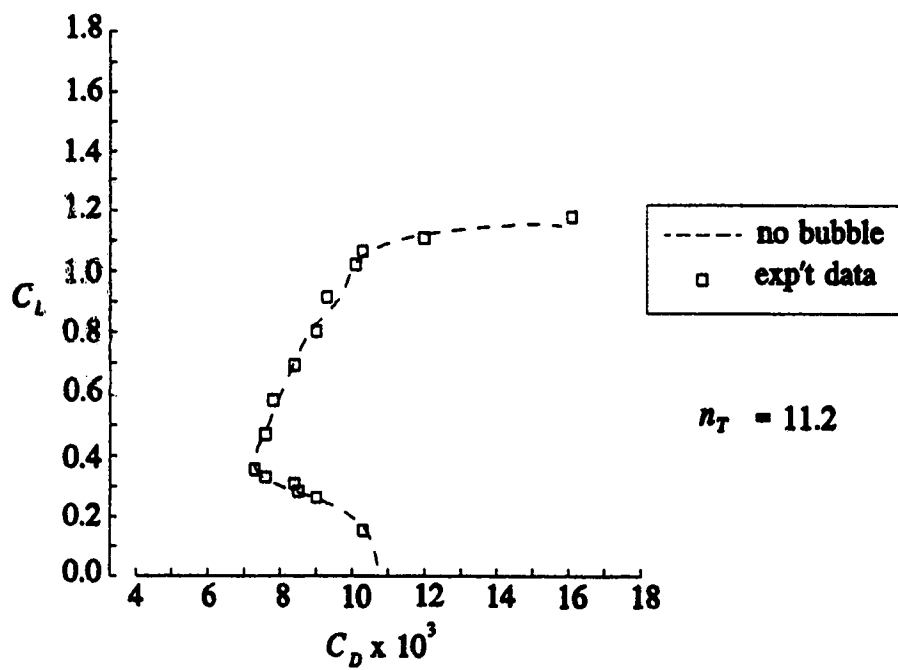


Figure 12 Eppler 387 airfoil at $Re_c = 0.46(10^6)$

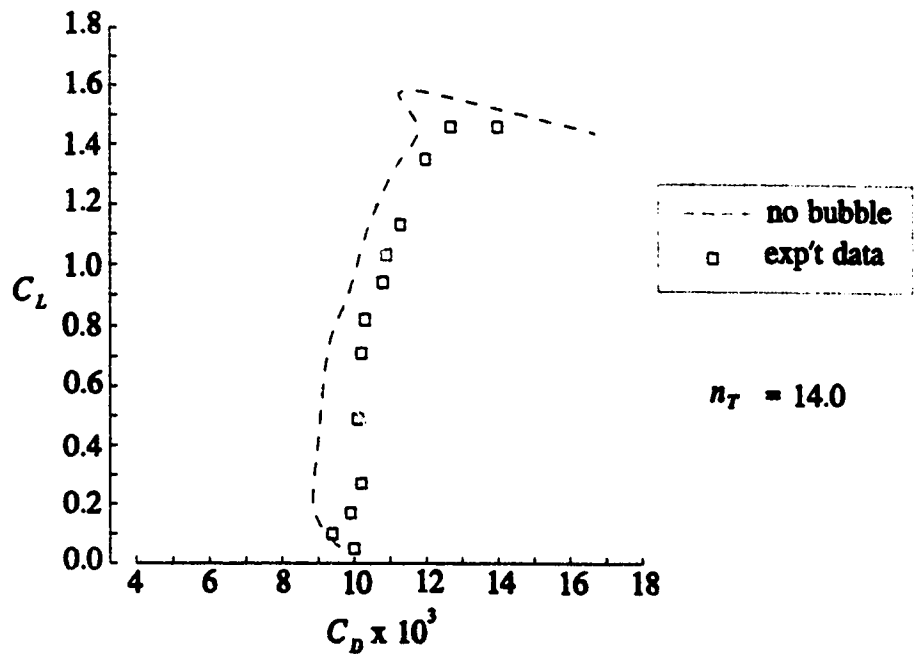


Figure 13 FX 66-17A-175 airfoil at $Re_c = 10^6$

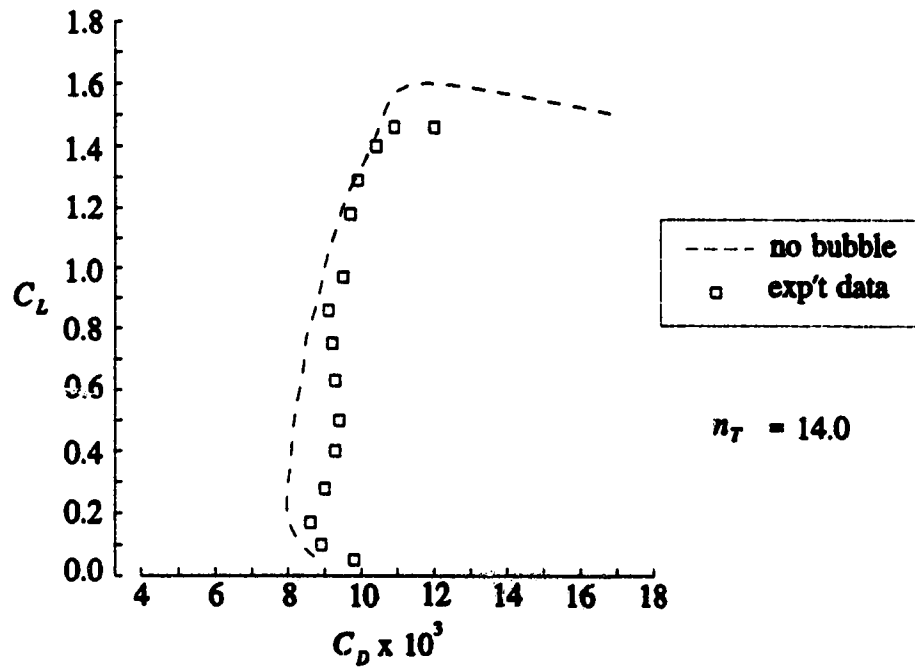


Figure 14 FX 66-17A-175 airfoil at $Re_c = 1.5(10^6)$

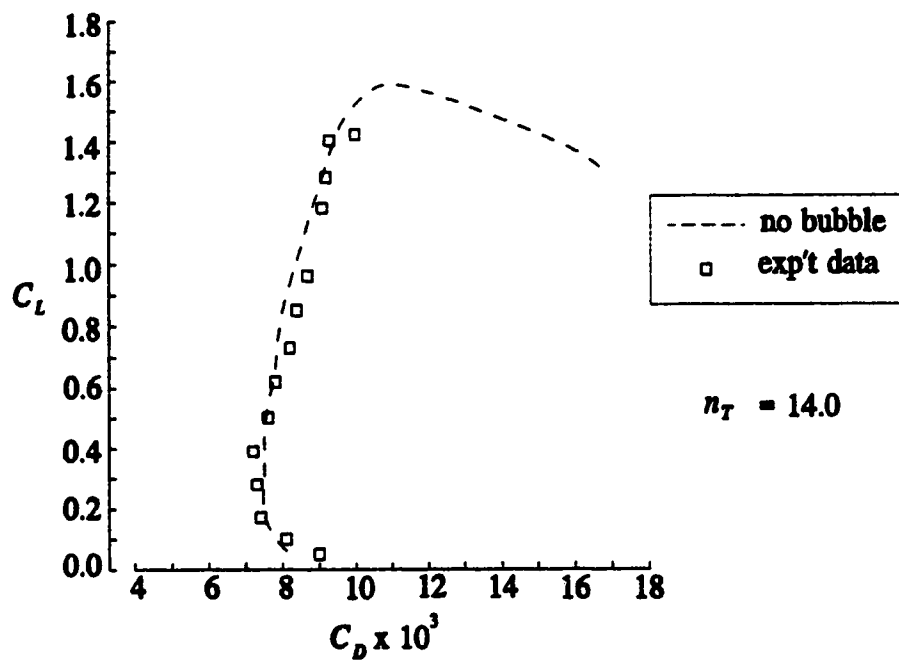


Figure 15 FX 66-17A-175 airfoil at $Re_c = 2(10^6)$

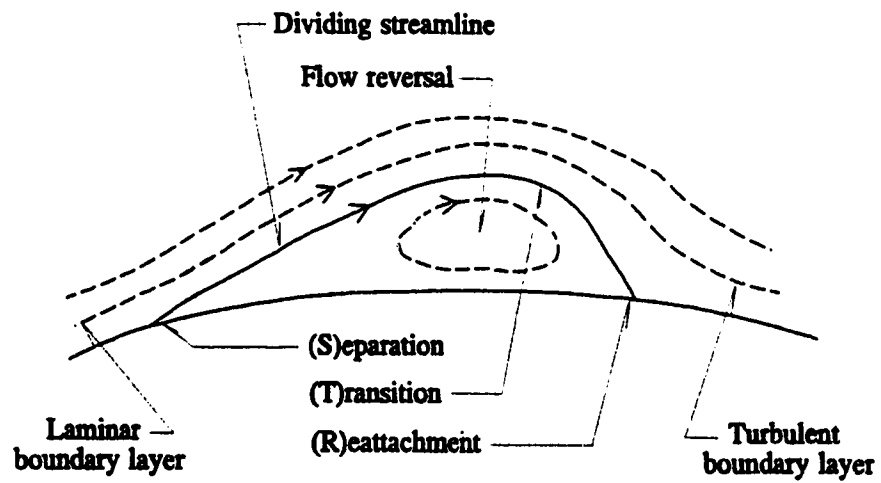


Figure 16 Flow structure of a separation bubble

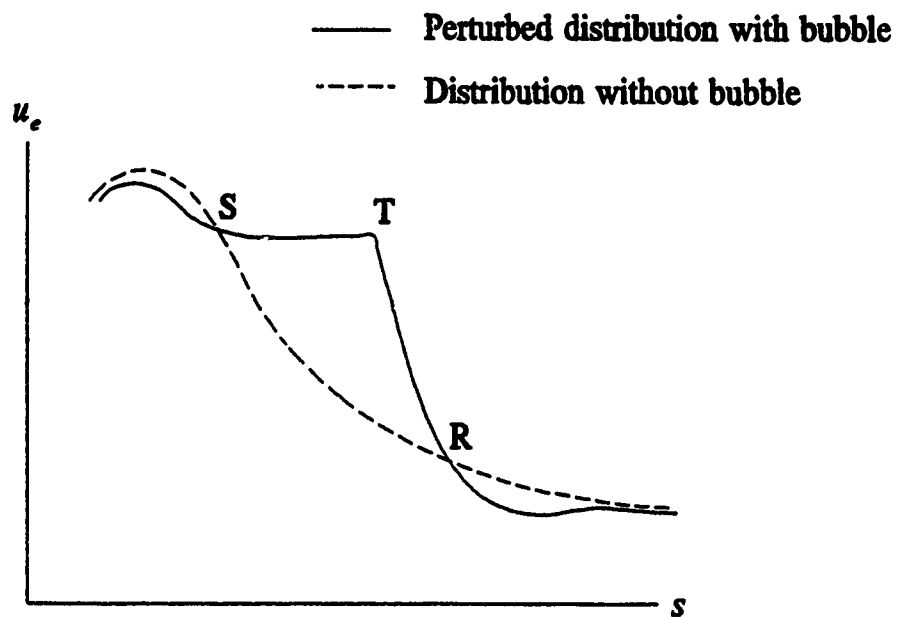


Figure 17 Velocity distribution near a separation bubble

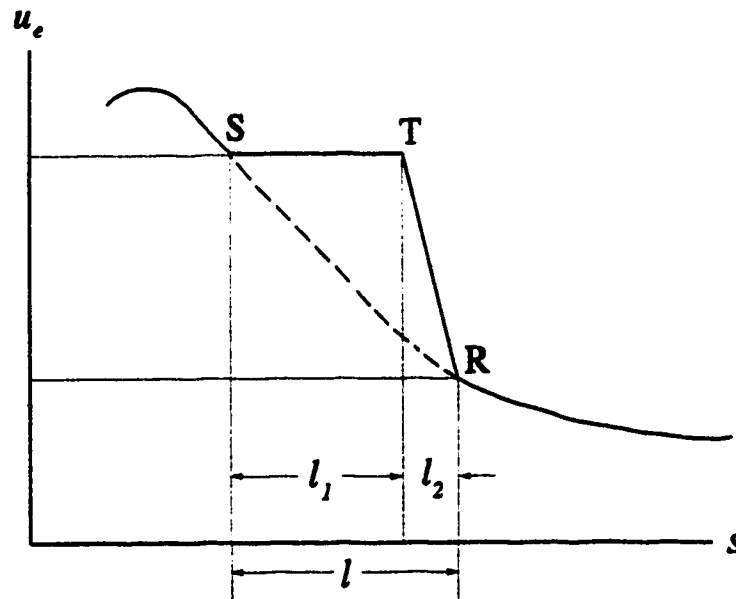


Figure 18 Velocity distribution of Horton's bubble model

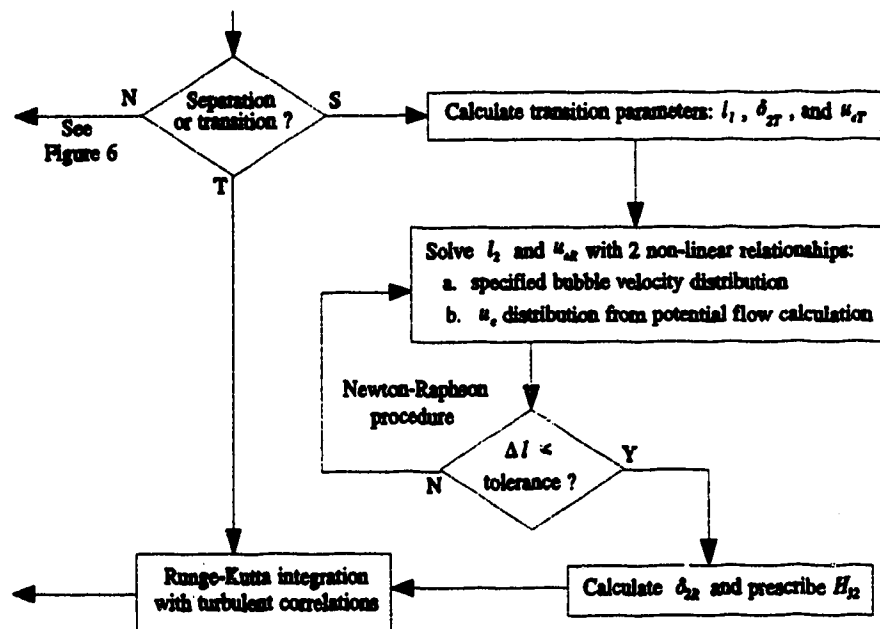


Figure 19 Bubble calculation flow chart

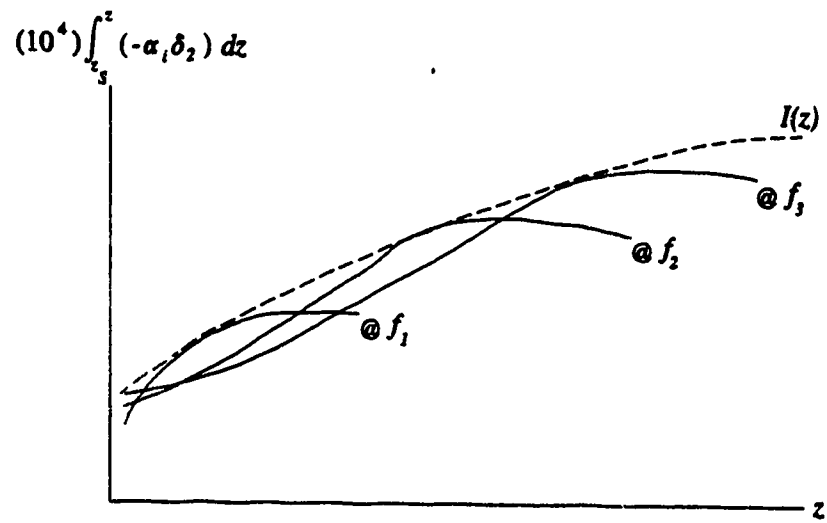


Figure 20 Expressing I in terms of z

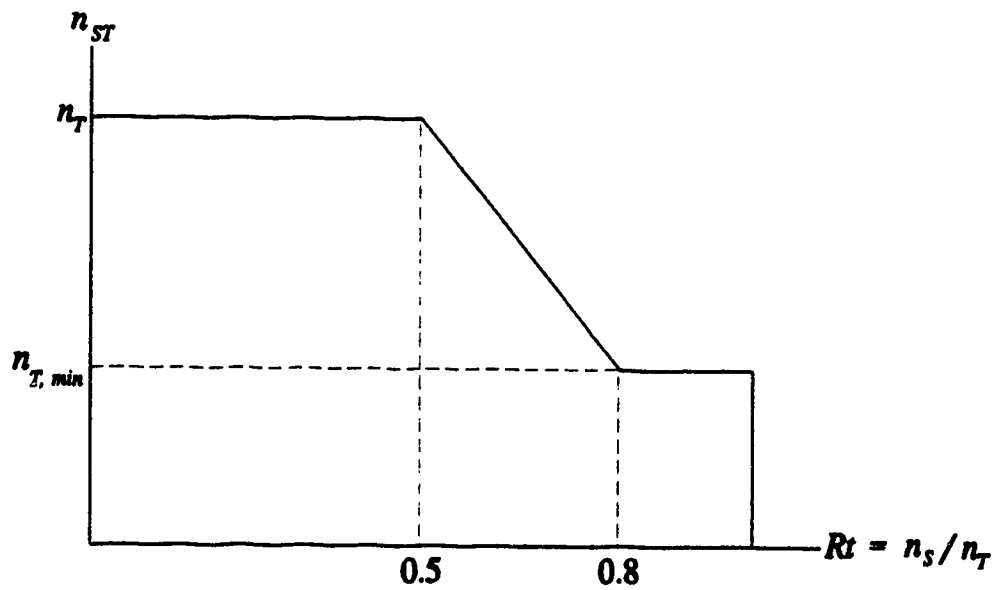


Figure 21 Bubble length parameter correction

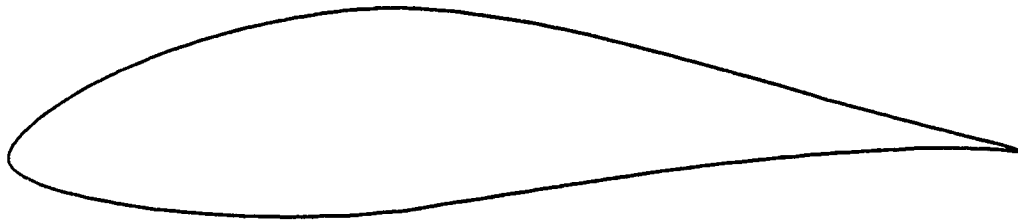


Figure 22 FX 66-S-196 V1 airfoil

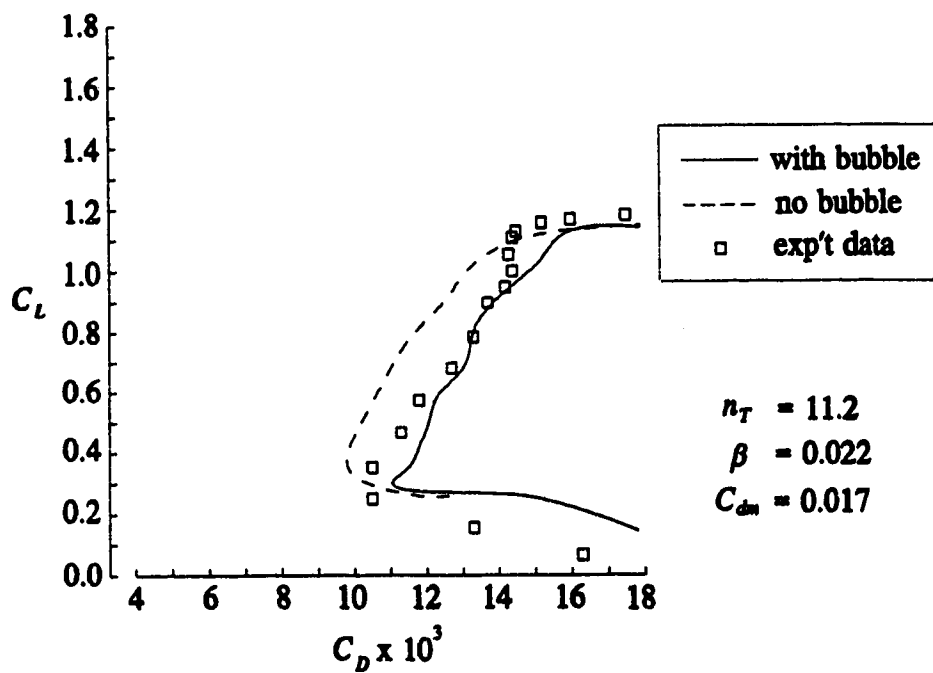


Figure 23 Eppler 387 airfoil at $Re_c = 0.2(10^6)$

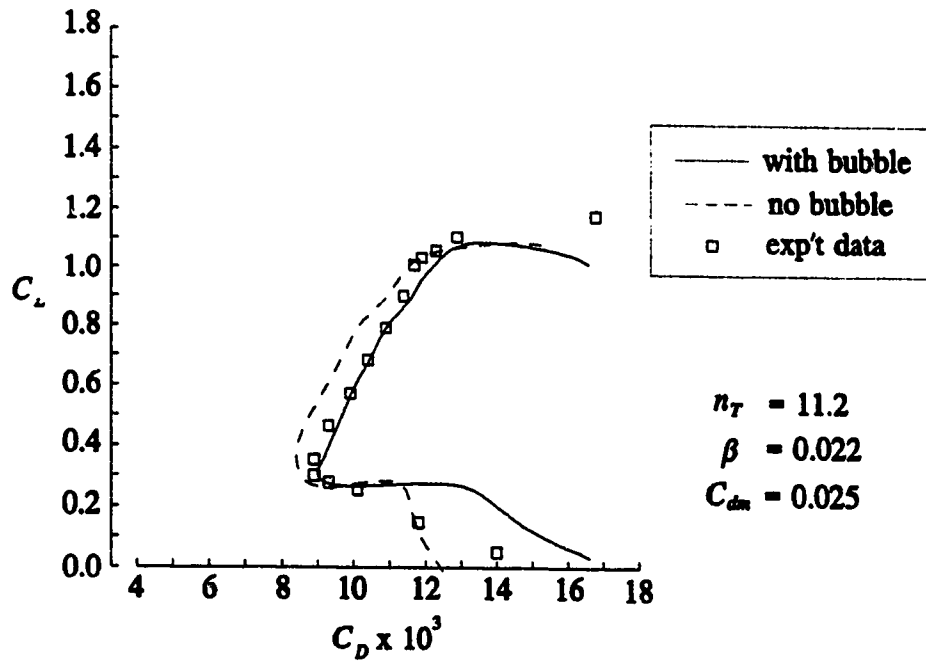


Figure 24 Eppler 387 airfoil at $Re_c = 0.3(10^6)$

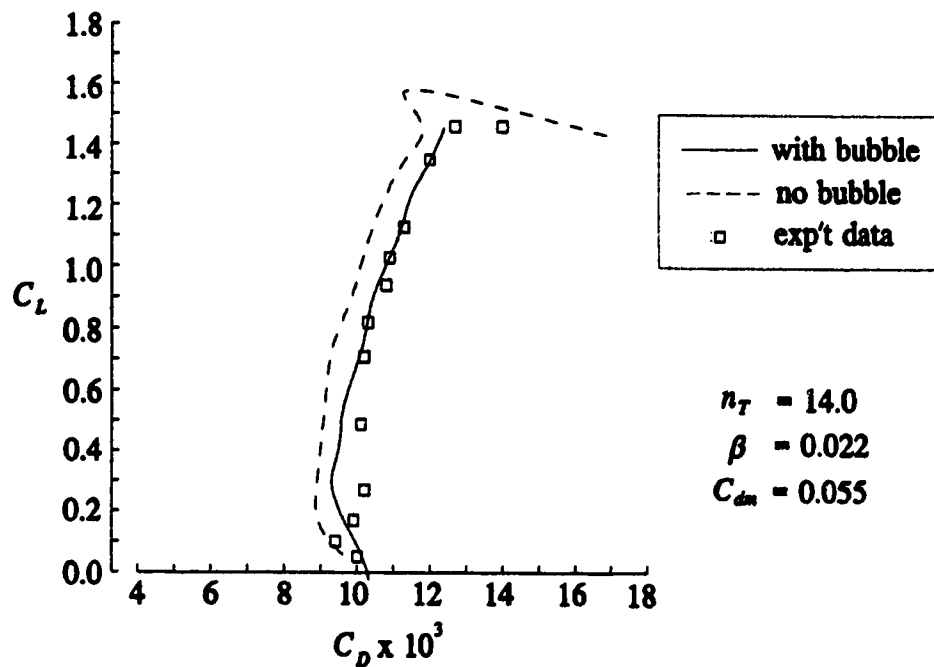


Figure 25 FX 66-17A-175 airfoil at $Re_c = 10^6$

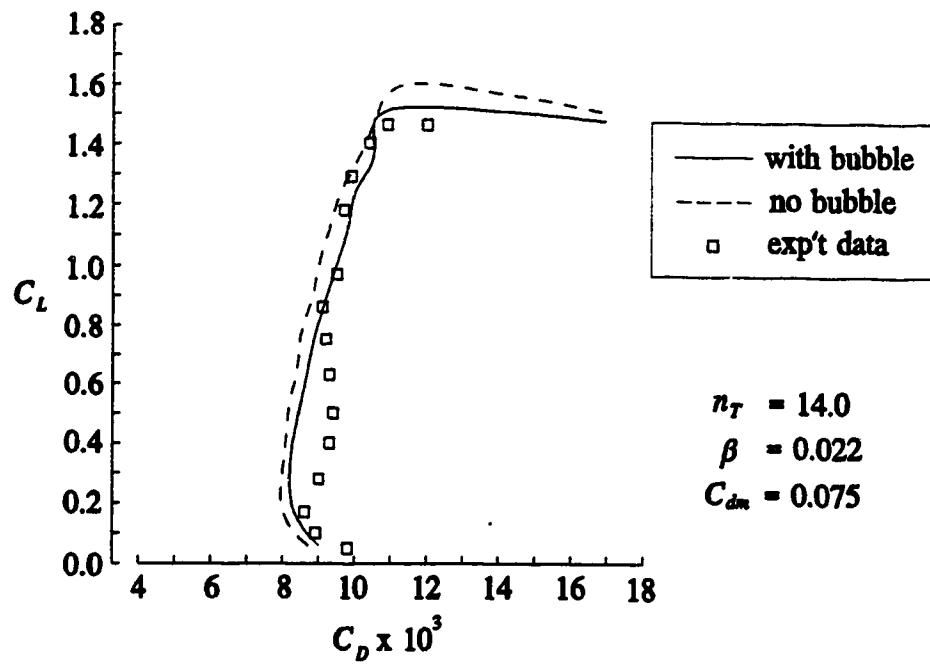


Figure 26 FX 66-17A-175 airfoil at $Re_c = 1.5(10^6)$

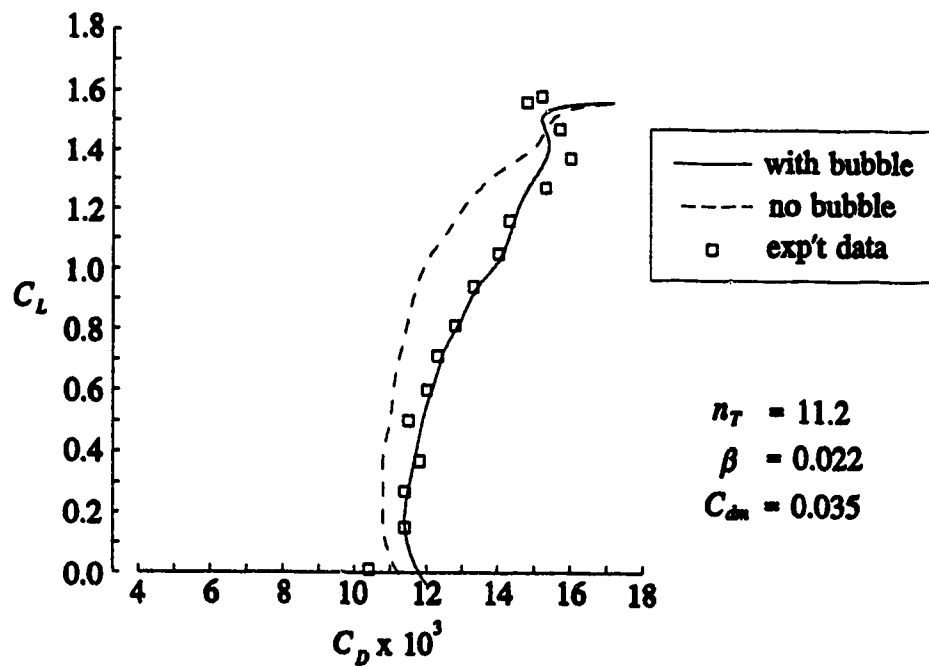


Figure 27 FX 66-S-196 V1 airfoil at $Re_c = 0.5(10^6)$

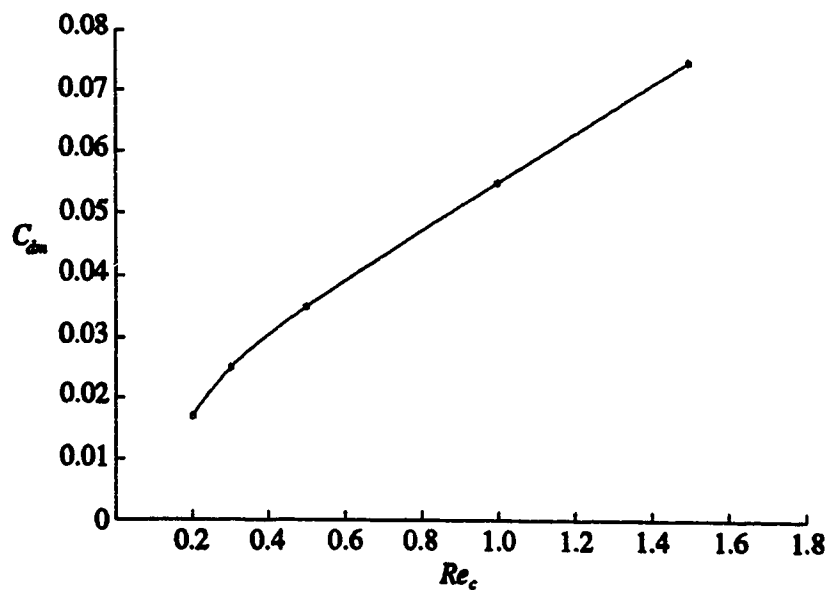


Figure 28 The correlations between C_{dm} and Re_c

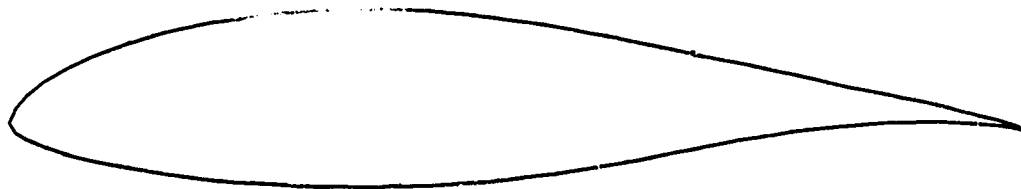


Figure 29 FX 61-163 airfoil

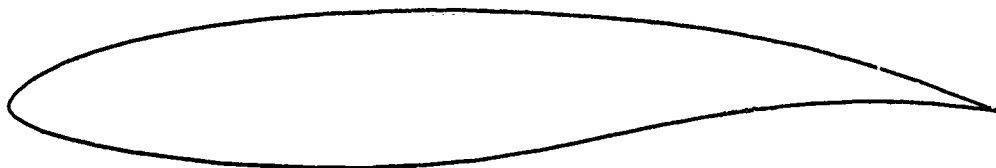


Figure 30 Eppler 403 airfoil

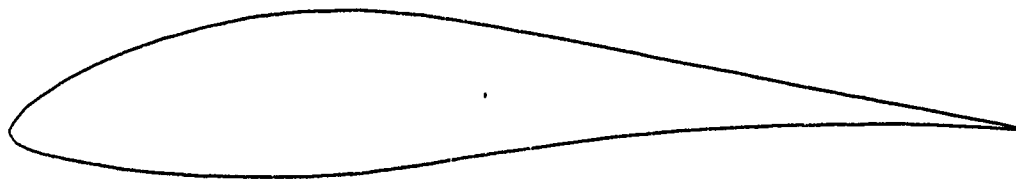


Figure 31 FX S02/1-158 airfoil

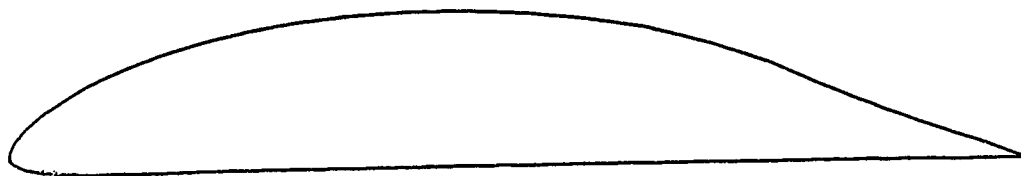


Figure 32 UAG-88-143 airfoil

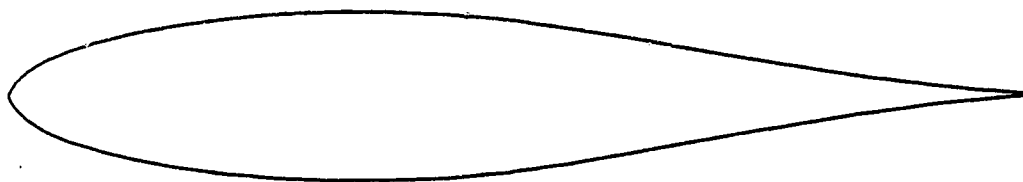


Figure 33 FX LV-152 airfoil

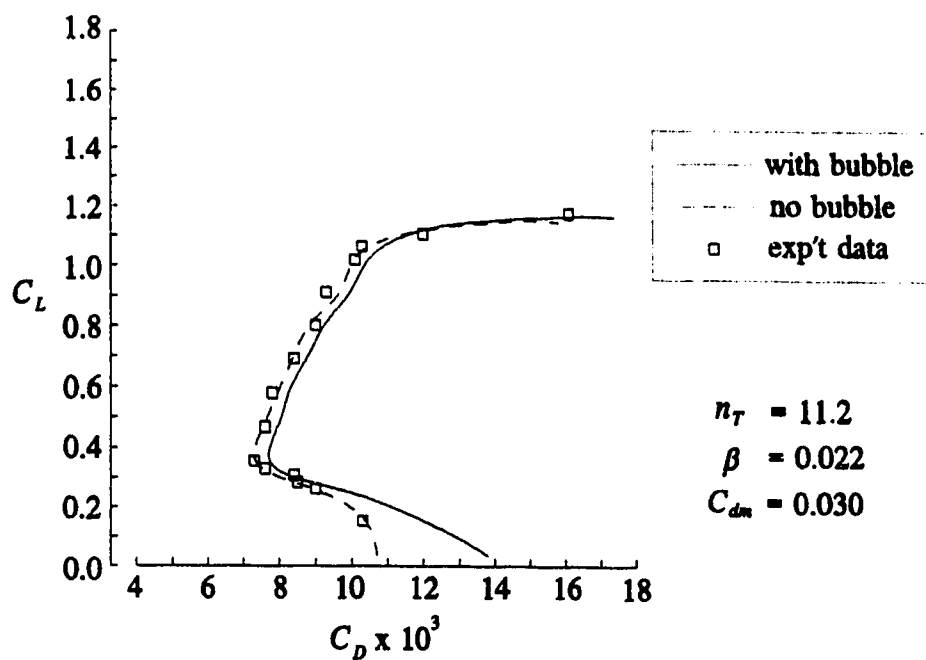


Figure 34 Eppler 387 airfoil at $Re_c = 0.46(10^6)$

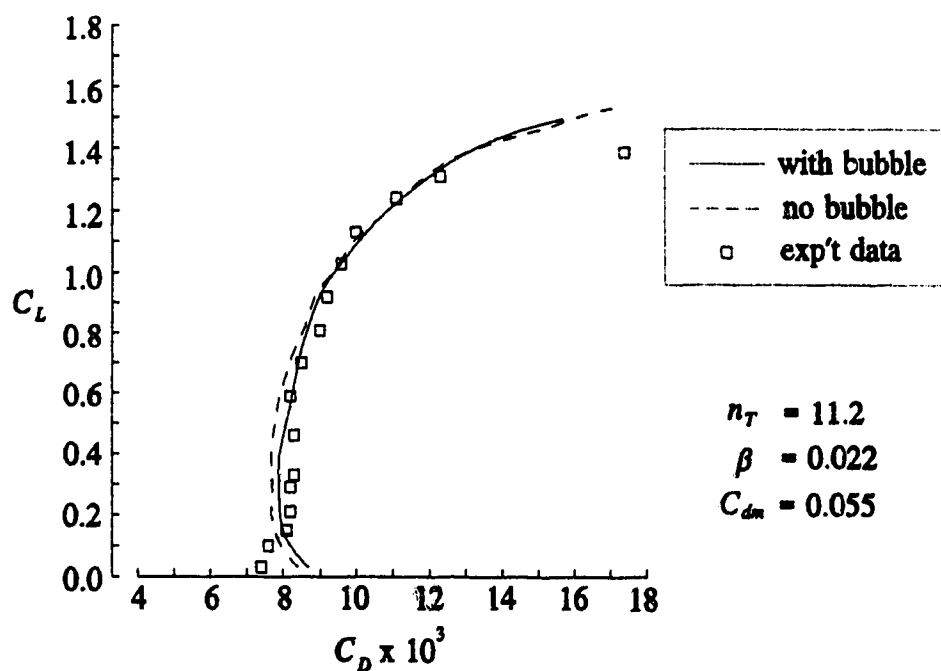


Figure 35 FX 61-163 airfoil at $Re_c = 10^6$

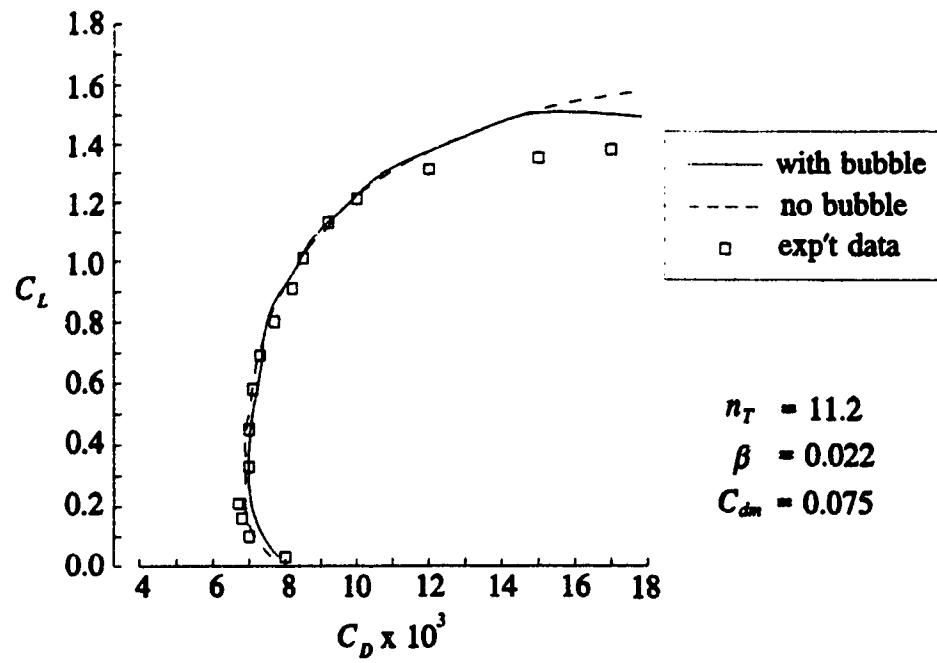


Figure 36 FX 61-163 airfoil at $Re_c = 1.5(10^6)$

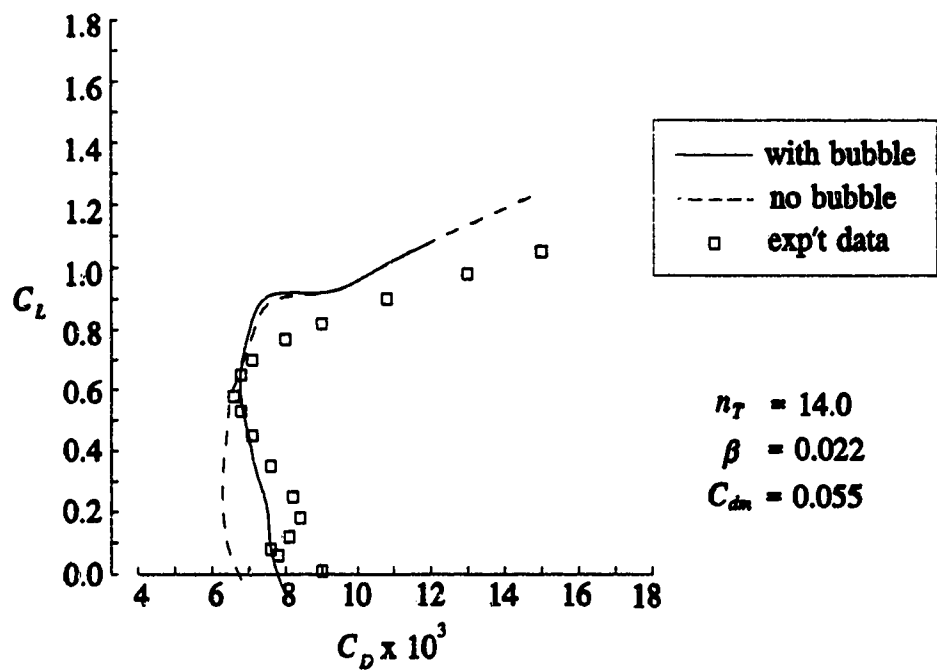


Figure 37 Eppler 403 airfoil at $Re_c = 10^6$

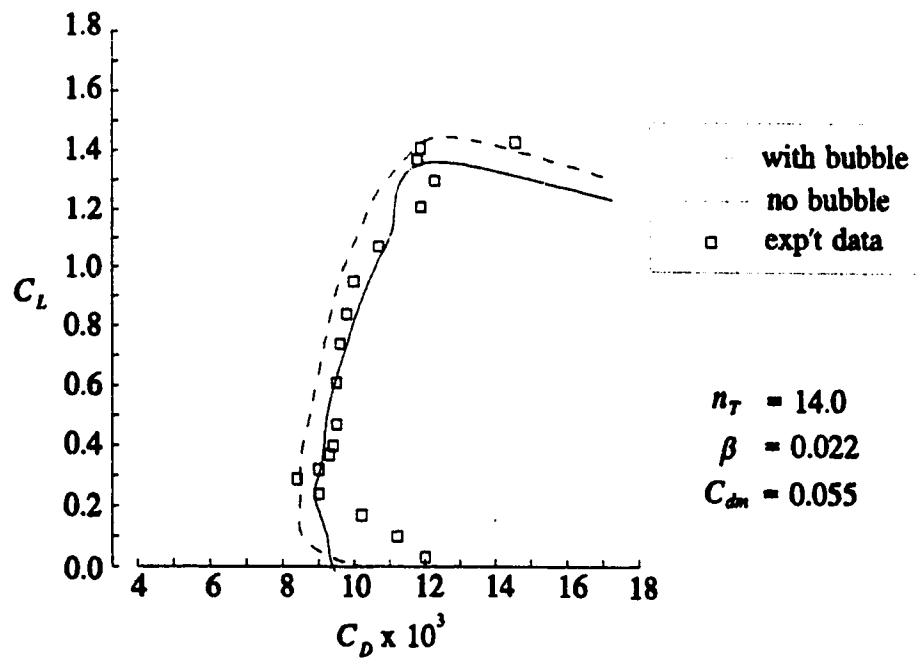


Figure 38 FX S02/1-158 airfoil at $Re_c = 10^6$

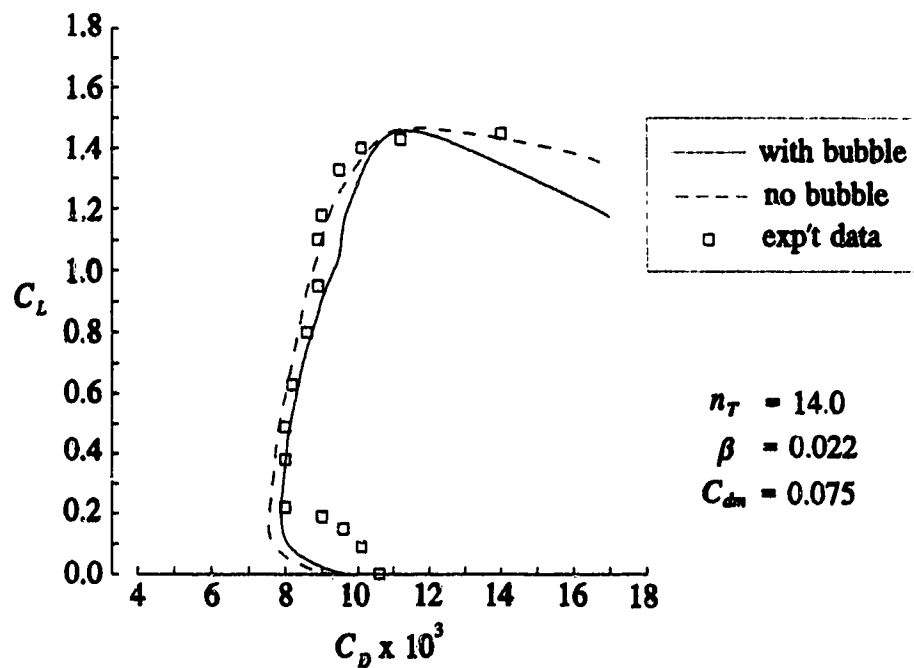


Figure 39 FX S02/1-158 airfoil at $Re_c = 1.5(10^6)$

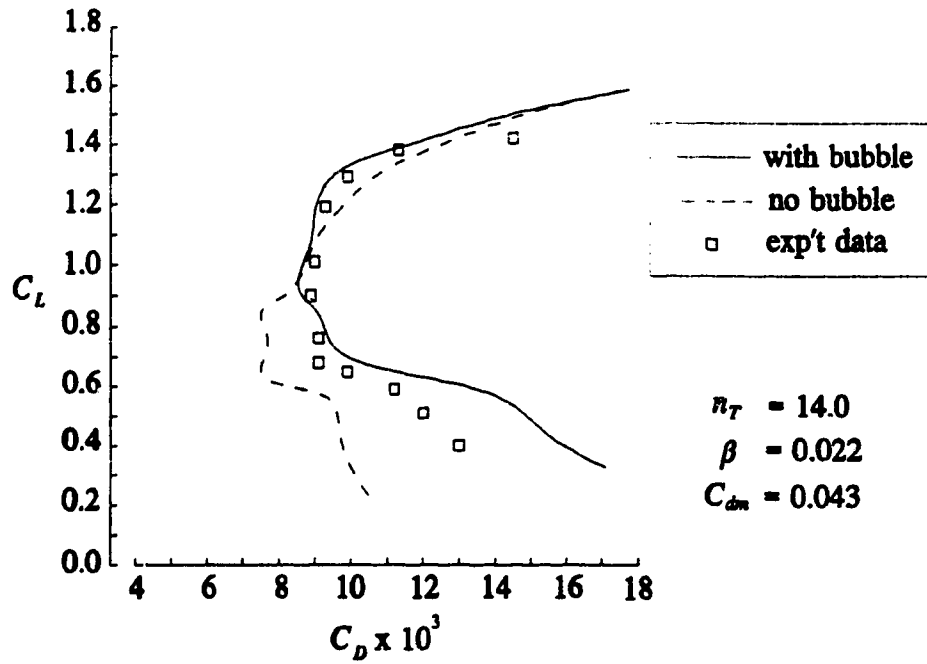


Figure 40 UAG 88-143/20 airfoil at $Re_c = 0.69(10^6)$

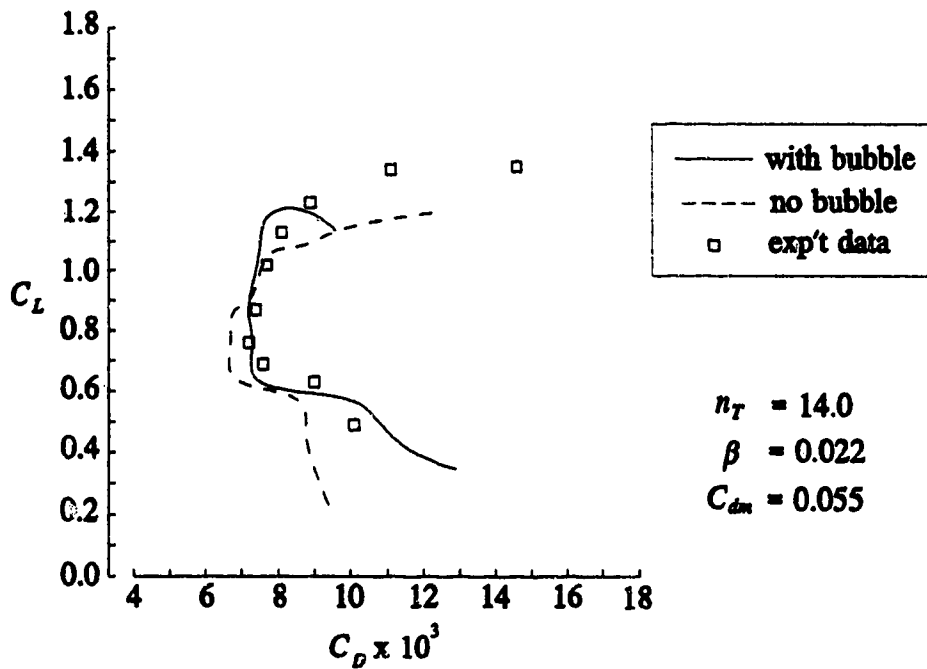


Figure 41 UAC 88-143/20 airfoil at $Re_c = 10^6$

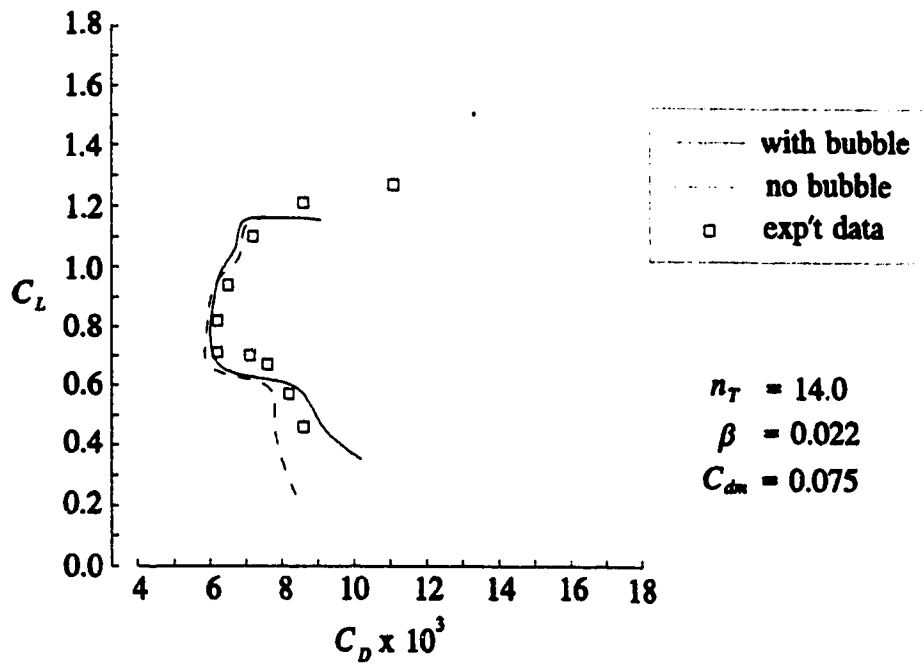


Figure 42 UAG 88-143/20 airfoil at $Re_c = 1.5(10^6)$

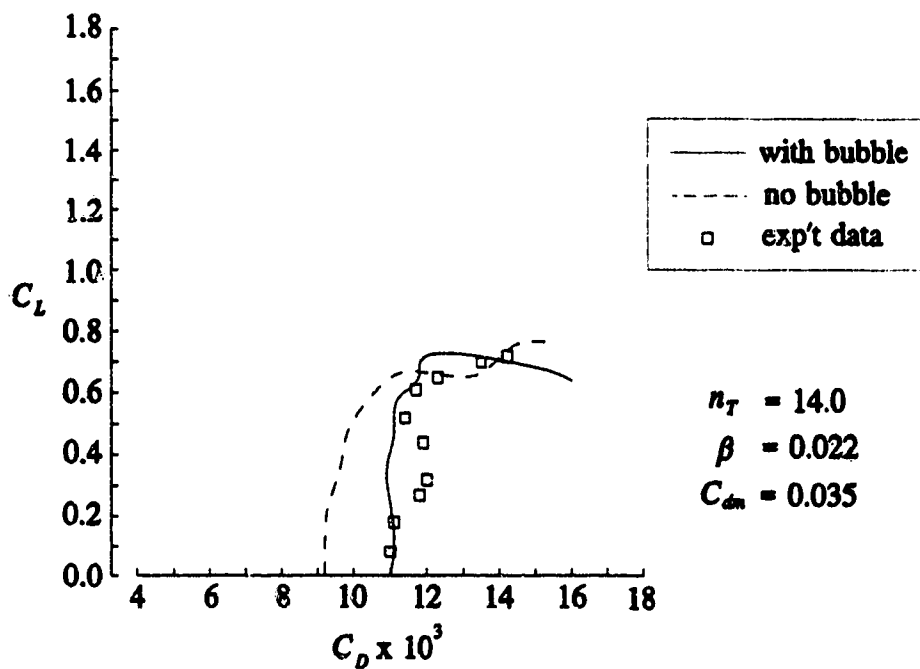


Figure 43 FX LV 152 airfoil at $Re_c = 0.5(10^6)$

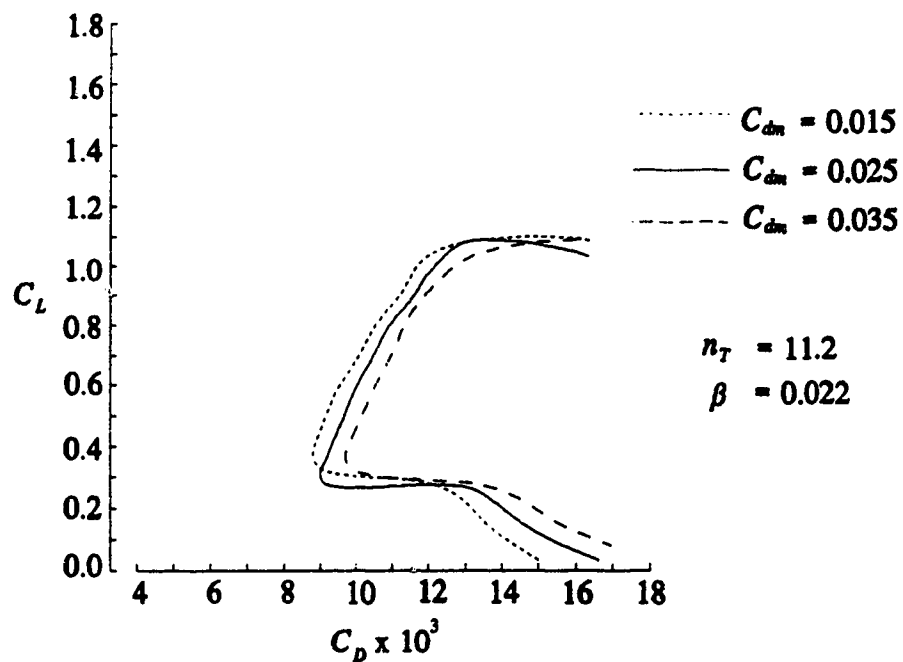


Figure 44 Effect of C_{dm} value on the drag prediction of the Eppler 387 airfoil at $Re_c = 0.3(10^6)$

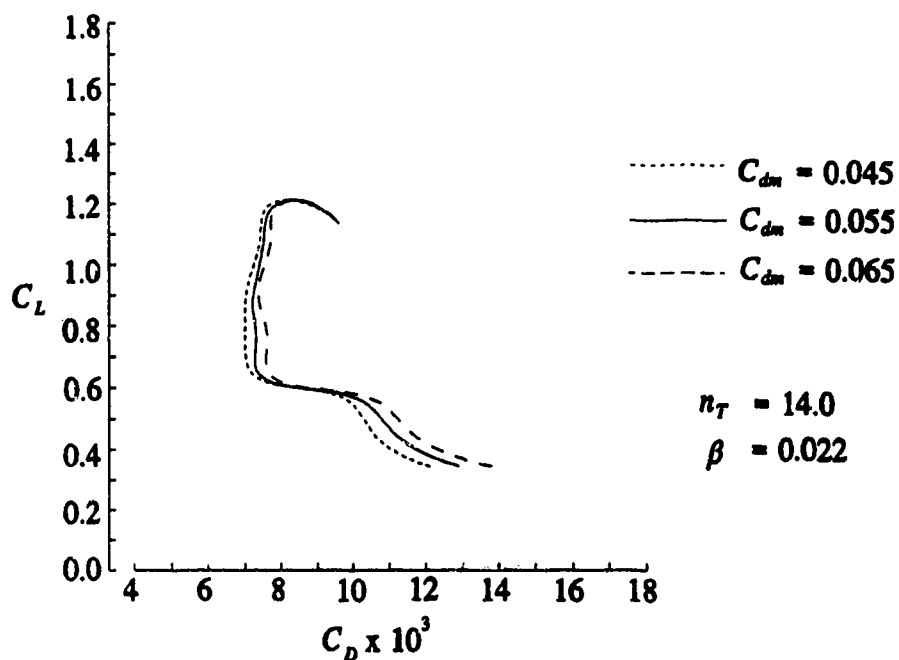


Figure 45 Effect of C_{dm} value on the drag prediction of the UAG 88-143/20 airfoil at $Re_c = 10^6$

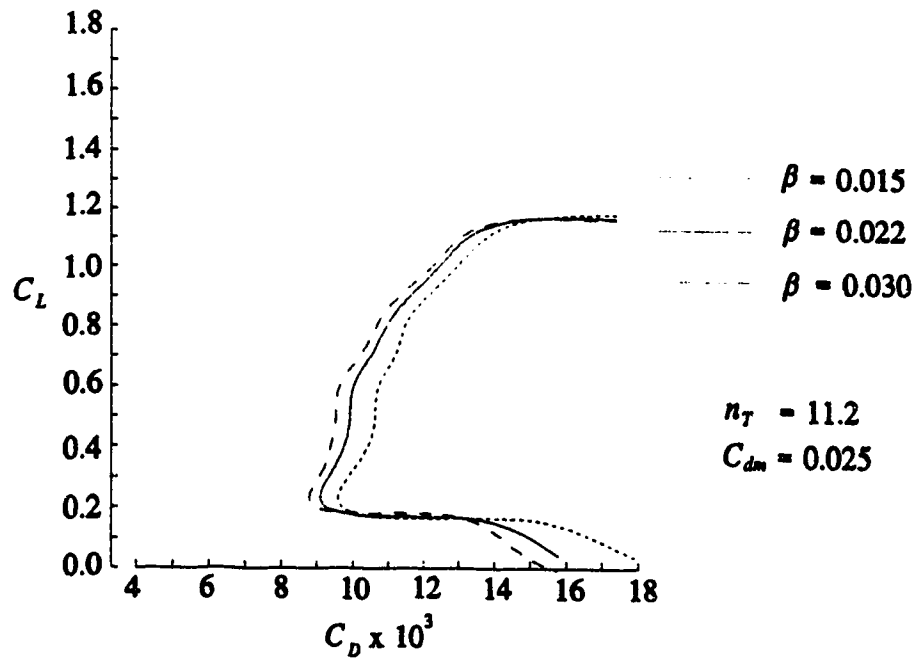


Figure 46 Effect of β value on the drag prediction of the Eppler 387 airfoil at $Re_c = 0.3(10^6)$

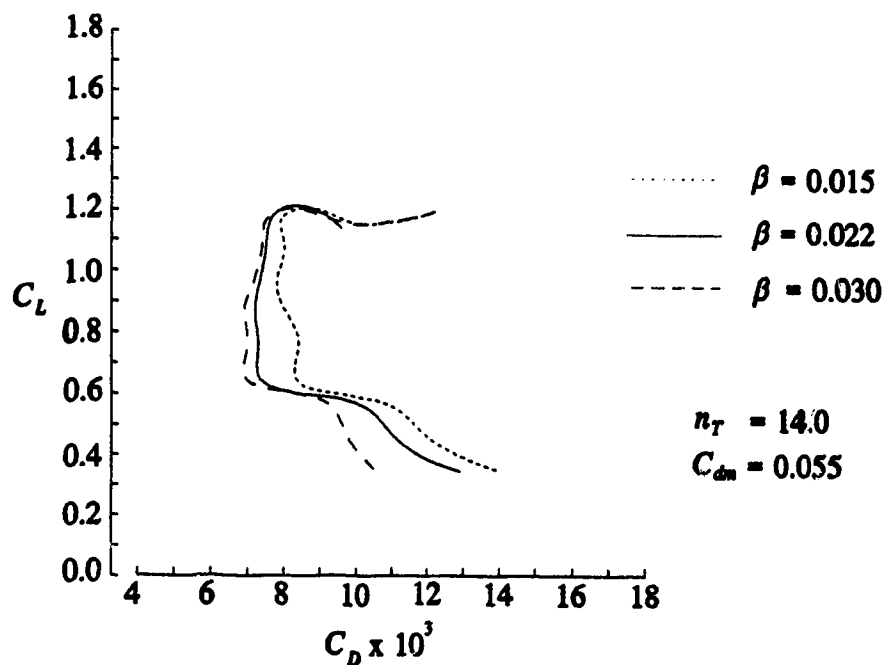


Figure 47 Effect of β value on the drag prediction of the UAG 88-143/20 airfoil at $Re_c = 10^6$

References

1. Marsden, D. J., "A High-Lift Wing Section for Light Aircraft," *Canadian Aeronautics and Space Journal*, Vol. 34, No. 1, March 1988, pp. 55-61.
2. Marsden, D. J., "Wind Tunnel Tests of an Ultralight Sailplane Wing Section," *Technical Soaring*, Vol. XIV, No. 1, 1990, pp. 7-12.
3. Drela, M., "Low-Reynolds-Number Airfoil Design for the M.I.T. Daedalus Prototype: A Case Study," *Journal of Aircraft*, Vol. 25, No. 8, 1988, pp. 724-732.
4. Lissaman, P. B. S., "Low-Reynolds-Number Airfoils," *Annual Review of Fluid Mechanics*, Vol. 15, 1983, pp. 223-239.
5. Maughmer, M. D., and Somers, D. M., "Design and Experimental Results for a High-Altitude, Long Endurance Airfoil," *Journal of Aircraft*, Vol. 26, No. 2, 1989, pp. 148-153.
6. Howard, R. M., "Airfoil Design for Endurance Unmanned Air Vehicles," *Journal of Aircraft*, Vol. 27, No. 11, 1990, pp. 971-973.
7. Selig, M. S., "The Design of Airfoils at Low Reynolds Numbers," AIAA Paper 85-0074, 1985.
8. Stratford, B. S., "The Prediction of Separation of the Turbulent Boundary Layer," *Journal of Fluid Mechanics*, Vol. 5, 1959, pp. 1-16.
9. Stratford, B. S., "An Experimental Flow with Zero Skin Friction throughout its Region of Pressure Rise," *Journal of Fluid Mechanics*, Vol. 5, 1959, pp. 17-35.
10. Eppler, R., "Airfoil Design and Data," Springer-Verlag, 1990.
11. Kennedy, J. L., "The Design and Analysis of Airfoil Sections," Ph. D. Thesis, University of Alberta, 1977.
12. Wortmann, F. X., "A Contribution to the Design of Laminar Profiles for Gliders and Helicopters," *Z. Flugwiss*, Vol. 3, No. 10, 1955, pp. 333-345, also in translation, Great Britain, Ministry of Aviation TIL/T.4903, 1960.
13. Liebeck, R. H., "Design of Subsonic Airfoils for High Lift," *Journal of Aircraft*, Vol. 15, No. 9, 1978, pp. 547-561.
14. McMasters, J. H. and Henderson, M. L., "Low-Speed Single-Element Airfoil Synthesis," NASA Conference Publication 2085, Part I, 1981, pp. 1-31.

15. Ward, J. W., "The Behaviour and Effects of Laminar Separation Bubbles on Aerofoils in Incompressible Flow," *Journal of the Royal Aeronautical Society*, Vol. 67, 1963, pp. 783-790.
16. Tani, I., "Low-Speed Flows Involving Bubble Separations," *Progress in Aeronautical Sciences*, Vol. 5, edited by D. Kuchemann and L. H. G. Sterne, Pergamon Press, New York, 1964, pp. 70-103.
17. Gad-el-Hak, M., "Control of Low-Speed Airfoil Aerodynamics," *AIAA Journal*, Vol. 28, No. 9, 1990, pp. 1537-1552.
18. Wortmann, F. X., "Progress in the Design of Low Drag Aerofoils," *Boundary Layer and Flow Control*, Vol. II, edited by G. V. Lachmann, Pergamon Press, pp. 748-770, 1967.
19. Horstmann, K. H., Quast, A., and Boermans, L. M. M., "Pneumatic Turbulators - A Device for Drag Reduction at Reynolds Numbers Below $5 * 10^6$," *AGARD CP 365*, 1984, pp. 20.1-20.19.
20. Pfenninger, W., Vemuru, C. S., Mangalam, S., and Evangelista, R., "Design of Low Reynolds Number Airfoils - II," *AIAA Paper 88-3764*, 1988.
21. Donovan, J. F. and Selig, M. S., "Low Reynolds Number Airfoil Design and Wind Tunnel Testing at Princeton University," *Proceedings of the Conference on Low Reynolds Number Aerodynamics*, edited by T. J. Mueller, University of Notre Dame, IN, 1989, pp. 33-51.
22. Mangalam, S. M., Bar-Sever, A., Zaman, K. B. M. Q., and Harvey, W. D., "Transition and Separation Control on a Low Reynolds Number Airfoil," *Proceedings of the International Conference on Aerodynamics at Low Reynolds Numbers*, Vol. I, Royal Aeronautical Society, London, 1986, pp. 10.1-10.19.
23. Miley, S. J., "On the Design of Airfoils for Low Reynolds Numbers," *Proceedings of the Second International Symposium on the Technology and Science of Low-Speed and Motorless Flight*, 1974, pp. 82-96.
24. Gibbings, J. C., Goksel, O. T., and Hall, D. J., "The Influence of Roughness Trips upon Boundary-Layer Transition. Part 1 Characteristic of Wire Trips," *Aeronautical Journal*, Vol. 90, October 1986, pp. 289-301.
25. Ingen, J. L. van and Boermans, L. M. M., "Aerodynamics at Low Reynolds Numbers: A Review of Theoretical and Experimental Research at Delft University of Technology," *Proceedings of the International Conference on Aerodynamics at Low Reynolds Numbers*, Vol. I, Royal Aeronautical Society, London, 1986, pp. 1.1-1.40.

26. Boermans, L. M. M. and Waibel, G., "Aerodynamic Design of the Standard Class Sailplane ASW-24," *Technical Soaring*, Vol. XIII, No. 3, 1989, pp. 72-83.
27. Kennedy, J. L. and Marsden, D. J.; "Potential Flow Velocity Distributions on Multi-Component Airfoil Sections," *Canadian Aeronautics and Space Journal*, Vol. 22, No. 5, 1976, pp. 243-256.
28. Toogood, R., Univ. of Alberta, private discussion.
29. Mokterian, F., and Modi, V. J., "Fluid Dynamics of Airfoils with Moving Surface Boundary-Layer Control," *Journal of Aircraft*, Vol. 25, No. 2, 1988, pp. 163-169.
30. Eppler, R., "Practische Berechnung Laminarer und Turbulenter Absauge - Grenzschichten," *Ingenieur Archiv*, Bd. 32, 1963, pp. 222-245.
31. Felsch, K. O., Geropp, D., and Walz, A., "Method for Turbulent Boundary Layer Prediction," *AFOSR IFP-Stanford Conference*, Vol. 1, 1968, pp. 170-176.
32. Drela, M. and Giles, M. B., "ISES: A Two-Dimensional Viscous Aerodynamic Design and Analysis Code," *AIAA Paper 87-0424*.
33. Dini, P., "A Computationally Efficient Modelling of Laminar Separation Bubbles," Ph. D. Thesis, Pennsylvania State University, 1990.
34. White, F. M., "Viscous Fluid Flow," McGraw-Hill, 1974.
35. Finlay, W., Univ. of Alberta, private discussion, 1990.
36. Arnal, D., "Description and Prediction of Transition in Two-Dimensional, Incompressible Flow," *AGARD Report 709*, 1984, pp. 2.1-2.71.
37. Gleyzes, C., Cousteix, J., and Bonnet, J. L., "A Calculation Method of Leading Edge Separation Bubbles," *II Symposium on Numerical and Physical Aspects of Aerodynamics Flows*, Long Beach, CA, January 1983.
38. Cousteix, J., "Three-Dimensional Boundary Layers. Introduction to Calculation Methods," *AGARD Report No. 741*, 1987, pp. 1.1-1.49.
39. Liu, C. Y. and Sandborn, V. A., "Evaluation of the Separation Properties of Laminar Boundary Layers," *Aeronautical Quarterly*, Vol. 19, 1968, pp. 149-154.
40. Curle, N. and Skan, S. W., "Approximate Methods for Predicting Separation Properties of Laminar Boundary Layer," *Aeronautical Quarterly*, Vol. 8, 1957, pp. 257-268.

41. Blascovich, J. D., "A Comparison of Separated Flow Airfoil Analysis Methods," *Journal of Aircraft*, Vol. 22, No. 3, 1985, pp. 208-215.
42. Squire, H. B. and Young, A. D., "The Calculation of the Profile Drag of Aerofoils," *Aeronautical Research Council R & M 1838*, 1937.
43. McGhee, R. J., Walker, B. S., and Millard, B. F., "Experimental Results for the Eppler 387 Airfoil at Low Reynolds Number in the Langley Low-Turbulence Pressure Tunnel," *NASA TM 4062*, 1988.
44. Althaus, D. and Wortmann, F. X., "Stuggarter Profilkatalog I," 1972.
45. Horton, H. P., "A Semi-empirical Theory for the Growth and Bursting of Laminar Separation Bubbles," *Aeronautical Research Council, C. P. No. 1073*, 1967.
46. Schmidt, G. S., "The Prediction of Transitional Separation Bubbles at Low Reynolds Numbers," *Ph. D. Dissertation, Univ. of Notre Dame*, 1986.
47. Fitzgerald, E. J. and Mueller, T. J., "Measurements in a Separation Bubble on an Airfoil Using Laser Velocimetry," *AIAA Journal*, Vol. 28, No. 4, 1990, pp. 584-592.
48. Roberts, W. B., "Calculation of Laminar Separation Bubbles and Their Effect on Airfoil Performance," *AIAA Journal*, Vol. 18, No. 1, 1980, pp. 25-31.
49. Coiro, D. and de Nicola, C., "Low Reynolds Number Flows: The Role of the Transition," *Memoria Presentata al X Congresso Nazionale AIDAA, Pisa, Sept. 1989*.
50. Ingen, J. L. van, "Transition, Pressure Gradient, Suction, Separation and Stability Theory," *AGARD CP 224*, 1977, pp. 20.1-20.15.
51. Boermans, L. M. M. and Selen, H. J. W., "Design and Tests of Airfoils for Sailplanes with an Application to the ASW-19B," *ICAS-Paper 82-5.5.2, Seattle, USA, 1982*.
52. Althaus, D. and Würz, W., "Wind Tunnel Tests of the UAG 88-143/20 Airfoil," *University of Stuttgart Internal Report*, 1991.